Sun-Induced Fluorescence as a Proxy of Primary Productivity across Vegetation Types and Climates

Mark Pickering [1], Alessandro Cescatti [2], and Gregory Duveiller [2,3]

[1]JRC consultant, Ispra, Italy
[2]European Commission, Joint Research Centre, Ispra, Italy
[3]Max Planck Institute for Biogeochemistry, Jena, Germany

Correspondence: Mark.Pickering1@ext.ec.europa.eu, Alessandro.Cescatti@ec.europa.eu, GDuveiller@bgc-jena.mpg.de

Abstract.

Sun-induced chlorophyll fluorescence (SIF) retrieved from satellites has shown potential as a remote sensing proxy for gross primary productivity (GPP). However, to fully exploit the potential of this signal, the robustness and stability of the SIF-GPP relationship across vegetation types and climates must be assessed. For this purpose, current studies have been limited by the availability of SIF datasets with sufficient spatial resolution to disentangle the signal between different vegetation cover types. To overcome this limitation ~~our~~ the analysis uses GOME-2 (Global Ozone Monitoring Experiment 2) SIF retrievals, downscaled to a resolution of $0.05°$ (~ 5km) to explore the relationship between SIF and FLUXCOM GPP (GPP_{FX}), a data-driven dataset of primary productivity obtained by upscaling flux-tower measurements. The high resolution of the downscaled SIF (SIF_{DS}) dataset allows the relationships to be broken down by vegetation cover for separate climate zones, thus enabling a confrontation between GPP and SIF at fine granularity~~, and the comparison and categorisation of vegetation covers based on the SIF_{DS}-GPP_{FX} response.~~. This analysis first investigates the spatial and temporal relationships between FLUXCOM GPP and downscaled SIF at a global scale. ~~Divergences and convergences between the two datasets are explored to see where high-resolution SIF can enhance our understanding of GPP.~~ A reasonably strong linear relationship is generally observed between SIF_{DS} and GPP_{FX} in all vegetation categories, and an analysis of covariance (ANCOVA) shows that the spatial response is similar between certain plant traits, with some distinction between herbaceous and woody vegetation, and notable exceptions, such as equatorial broadleaf forests~~, and continental needleleaf forests, and distinction between woody and herbaceous vegetation. The temporal relationship between SIF_{DS} and GPP_{FX}, within a growing season, is shown to be the strongest, followed by the spatial relationship and finally the SIF_{DS}-GPP_{FX} trend between growing seasons. Whilst a linear spatial relationship is generally observed between SIF_{DS} and GPP_{FX} in all vegetation categories, geographical~~. Geographical regions of non-linearity suggest where SIF_{DS} could potentially provide information about ecosystem dynamics that are not represented in the FLUXCOM GPP dataset. With the demonstration of downscaled SIF as a proxy for GPP, the response of SIF_{DS} to short-term fluctuations in several meteorological variables is analysed ~~, and the utility of SIF_{DS} as a measure of environmental stress explored. For a broad range of land cover categories, the most significant~~ and the most significant short-term environmental driving and limiting meteorological variables ~~are determinedand vegetation~~ determined. Vegetation groupings of similar SIF-meteo response reinforce the vegetation categorisations suggested by the ~~SIF-GPP ANCOVA~~ ANCOVA analysis.

This comparative exploration of two of the most recent products in carbon productivity estimation shows the value in downscaling SIF data, provides an independent probe of the FLUXCOM GPP model, enhances our understanding of the global SIF-GPP spatio-temporal relationship with a particular focus on the role of vegetation cover, and ~~demonstrates the utility of SIF as a measure of environmental stress.~~ explores the similarity of the SIF and GPP responses to meteorological fluctuations.

30 Additional analyses with alternative SIF and GPP datasets support these conclusions.

1 Introduction

Accurately quantifying the gross primary productivity (GPP) of vegetation systems across the globe is vital for modelling the future trajectories of atmospheric carbon fluxes and making projections regarding the Earth's climate. Indeed one of the largest sources of uncertainty in the carbon cycle is represented by the interaction between atmospheric carbon dioxide, climate and terrestrial ecosystem dynamics (Friedlingstein et al., 2019; Anav et al., 2015). Photosynthesis drives this interaction, with vegetation removing carbon from the atmosphere and investing it in growth, cell maintenance and respiration. In turn, photosynthesis is regulated by environmental conditions, and, as climates change, both the mean weather and its variability will change, impacting the productivity of vegetation systems (Seneviratne et al., 2012).

It is not possible to directly measure GPP at a global level, however many techniques have been developed to derive productivity at different scales using a range of data-driven or model-based approaches.Light use efficiency (LUE) models, for example, estimate GPP as a function of the absorbed photosynthetically active radiation (APAR), the efficiency of utilising light in photosynthesis ϵ_{LUE} and the effect of climatic constraints, such as temperature (T) and precipitation (P):

~~GPP = ϵ_{LUE} x APAR x f(T) x f(P) (Ryu et al., 2019; Running et al., 2004; Zhang et al., 2017; Lee et al., 2013)~~

$$\text{GPP} = \epsilon_{\text{LUE}} \text{ x APAR x } f(\text{T}) \text{ x } f(\text{P}) \tag{1}$$

(Ryu et al., 2019; Running et al., 2004; Zhang et al., 2017; Lee et al., 2013; Pei et al., 2022).

A relevant assessment based on a process-oriented ensemble, known as TRENDY, provides a model-based estimation of global GPP ranging between $83 - 172$ PgC yr^{-1}, with the wide range of values highly dependent on the model assumptions. Eddy covariance sites, or flux towers, provide the most accurate ways of measuring carbon fluxes at ecosystem scale, through the systematic observation of the net ecosystem exchange of ~~CO2~~ CO_2. These measurements have been standardised and made available thanks to the FLUXNET initiative that is linking different continental networks of eddy covariance towers (Baldocchi et al., 2001). The FLUXCOM project has upscaled FLUXNET data to a global estimate of GPP using machine learning methods to integrate site-level observations, satellite remote sensing information, and meteorological data (Tramontana et al., 2016). Whilst FLUXCOM is a large step forward in estimating GPP at a global level, it is not without its limitations and uncertainties. In fact, the various FLUXCOM GPP estimates use an ensemble of different machine learning methods and data inputs, which result in a broad spread of mean global GPP estimates among the ensemble members between $108 - 130$ PgC yr^{-1}. A comparative study between FLUXCOM and TRENDY finds that for 70% of the globe at least the 9 out of 16 TRENDY models fall outside the FLUXCOM range (Jung et al., 2020).

In recent years, sun-induced chlorophyll-*a* fluorescence (SIF), retrieved from space-based instruments, has grown in use as a remotely sensed proxy for GPP, in addition to more traditional remote proxies such as spectral vegetation indices ~~(Ryu et al., 2019; Porcar-C~~ (Frankenberg et al., 2011a; Joiner et al., 2011; Porcar-Castell et al., 2014). This fluorescent light - resulting from the re-emission by leaves of incident photons at lower energy - is considered to be the mechanism developed by plants to respond near-instantaneously to rapid perturbations in the environmental conditions of light ~~, temperatureand water availability (Frankenberg and Berry, 2~~ and temperature, with the SIF yield also dependent on biophysical conditions such as the concentration of the CO_2-fixing enzyme Rubisco and drought stress (Frankenberg and Berry, 2017; Ryu et al., 2019). The SIF flux can similarly be expressed

65 in terms of the absorbed incident radiation and the efficiency with which this radiation is converted into fluorescent radiation, ϵ_F: ~~$SIF = \epsilon_F \times \epsilon_{esc} \times APAR$~~

$$SIF = \epsilon_F \times \epsilon_{esc} \times APAR \tag{2}$$

where the term, ϵ_{esc}, accounts for the efficiency of photons to escape re-absorption and scattering by other leaves in the canopy (Lee et al., 2013). Rearranging the equations for instantaneous SIF and GPP fluxes: ~~$GPP = \dfrac{\epsilon_{LUE}}{\epsilon_F \epsilon_{esc}} \times SIF$~~

70
$$GPP = \frac{\epsilon_{LUE}}{\epsilon_F \times \epsilon_{esc}} \times SIF \tag{3}$$

we see that under conditions in which the various conversion efficiencies remain constant, there is a linear relationship between SIF and GPP. Whilst at small spatio-temporal timescales, where leaf chemistry is particularly sensitive to changes in absorbed photosynthetically active radiation and the fraction of fluoresced photons escaping from the canopy, there is evidence for the divergence of SIF and GPP from linearity, it appears that the broader canopy-scale relationship smooths over these non-

75 linearities (Magney et al., 2020). Indeed, there is a substantial body of evidence that shows that SIF, measured from space-based instruments, is positively correlated with leaf photochemistry, often exhibiting a generally linear relationship in both space and time, and across spatio-temporal scales (Zhang et al., 2016; Sun et al., 2018; Magney et al., 2020). However, this SIF-GPP relationship may exhibit some dependency on the vegetation type, for example through the canopy structure that is affecting ϵ_{esc}, as well as the leaf photochemical properties and external conditions, for example climate drivers. Due to the relatively fast

80 response of SIF and close link to leaf photochemistry, compared to other remote indicators of greenness, such as NDVI, SIF has the potential to be an indicator of environmental stress for the plant photosystem (Walther et al., 2019; Jiao et al., 2019).

There is currently no orbiting satellite designed explicitly to directly measure SIF from space. The first that will do so is the exploratory mission FLEX, scheduled for launch in ~~2023~~ the coming years (Coppo et al., 2017). In the meanwhile, SIF has been retrieved from other instruments designed for measuring the atmosphere greenhouse gas concentration, namely GOSAT,

85 SCIAMACHY, the Global Ozone Monitoring Experiment-2 (GOME-2), the Orbiting Carbon Observatory 2 (OCO-2) and the TROPO-spheric Monitoring Instrument (TROPOMI) (Guanter et al., 2012; Joiner et al., 2012, 2013; Sun et al., 2018; Köhler et al., 2018b; . However, several issues hamper the use of these data for the quantification of terrestrial GPP. First, some instruments (GOSAT, OCO-2) are sampling the surface, leaving wide gaps between different satellite overpasses. Second, the time series of observations is shorter than desired for carbon science, especially for the more recent instruments (e.g. OCO-2 and TROPOMI). Third,

90 most have a spatial resolution that is too coarse to isolate homogeneous vegetation patches of distinct land cover types.

Efforts have been made to improve the resolution and coverage of SIF datasets by combining SIF data with other high resolution remote sensing data ~~(Gentine and Alemohammad, 2018; Li and Xiao, 2019; Zhang et al., 2018a; Yu et al., 2018)~~(Gentine and Alemoh . These approaches generally rely on statistical inference, through machine learning methods. A ~~recent~~ downscaling methodology, based on a light use efficiency model, combines the GOME-2 data with several explanatory biophysical variables in a

95 process oriented scheme. The resulting dataset has a spatial resolution of $0.05°$ (5km) and is therefore at a scale relevant to studies of land cover at global scale (Duveiller et al., 2020; Duveiller and Cescatti, 2016). This model ensures that the downscaling method is grounded ~~on a biophysical~~ in theory whilst also preserving the GOME-2 signal. Downscaling the SIF in

this way results in a high resolution dataset with a reasonably long archive, improving accuracy in the exploration of the SIF relationship with vegetation cover.

100   If downscaled sun-induced fluorescence is to be used as a proxy for ecosystem productivity ~~or as a measure of environmental stress,~~ it is important to understand the spatial and temporal relationships between SIF and the current state-of-the-art GPP datasets at a global scale, and in particular understand how they deviate for differing vegetation covers and climate zones. To this end, this paper serves several purposes. Firstly, the analysis provides a thorough test of the utility of the downscaling method to reproduce known SIF-GPP patterns, in particular through the spatio-temporal correlation between downscaled SIF and FLUX-

105 COM GPP. Exploring variations in the FLUXCOM GPP with an independent SIF dataset, often likewise regarded as a proxy to GPP, helps to probe its strengths and limitations through areas of coherence and divergence. Similarly, comparisons with alternative SIF and GPP products such as TROPOMI SIF (Guanter et al., 2021) and FluxSat GPP (Joiner and Yoshida, 2021) are provided in an appendix, in order to ensure the consistency and robustness of the conclusions. Second, as a global, high-resolution investigation into the SIF-GPP relationship, the analysis allows us to learn more about the differing spatial linear

110 relationship between SIF and GPP and their variation in nature with a particular focus on similarities and differences between vegetation covers. This allows the determination of which vegetation covers have a similar SIF-GPP response, and for which vegetation covers care should be taken in the use of SIF as a proxy for GPP. Finally, having established the spatio-temporal relationship between the downscaled SIF and the FLUXCOM GPP, the paper investigates the ~~potential~~ response of downscaled SIF ~~as a global measure of environmental stress~~ to fluctuations in several meteorological factors, in the process determining

115 the most significant driving and limiting meteorological factors in monthly SIF fluctuations. By utilising the high resolution of the downscaled SIF, it is possible to understand with improved confidence the extent to which vegetation cover plays a role in these relationships using dedicated techniques (e.g. Álvaro Moreno-Martínez et al., 2018).

2   Data

2.1   Vegetation cover data

120 The data relating to the vegetation cover of each pixel is derived from the Copernicus Climate Change Service (C3S) via the climate data store platform, with the data created by the ESA CCI program (CCI, 2017; Defourny, 2019). The land cover classes are converted to vegetation covers, as used by dynamic global vegetation models, whilst aggregating the data to a spatial resolution of $0.05°$. The following vegetation covers are considered: grassland = 'GRA', crops = 'CRO', evergreen broad-leaf forest = 'EBF', deciduous broad-leaf forest = 'DBF', evergreen needle-leaf forest = 'ENF', and deciduous needle-leaf forest =

125 'DNF'. To ensure a high homogeneity in the selected data, the dominant vegetation type must cover at least 75% of a pixel and with no change in the majority land cover classification over the considered years, 2007-2014.

2.2 Climate classification

The climate zone classification used in the analysis follows the Köppen-Geiger climate classification scheme (Kottek et al., 2006; Rubel and Kottek, 2010; Rubel et al., 2017). The classification maps are representative of the period 1986-2010 and are available at a spatial resolution of $0.0833°$ which are extrapolated via binomial interpolation to grid cells (referred to hereon as pixels) of $0.05°$.

Four broad categories are considered from this scheme: equatorial, arid, temperate and continental. Equatorial contains 'Group A' climate regions: areas where each month is above $18°C$ and with high precipitation. Arid regions are 'Group B' climates: areas defined by low precipitation. Temperate regions are 'Group C' climates: with the coldest month averaging $0 - 18°C$ and at least one month averaging more than $10°C$. Finally, continental regions are 'Group D' climates: at least one month must average below $0°C$ and at least one month above $10°C$. Figure 1 shows the spatial distribution of the global climate groupings and the dominant vegetation cover of the pixels considered in the analysis.
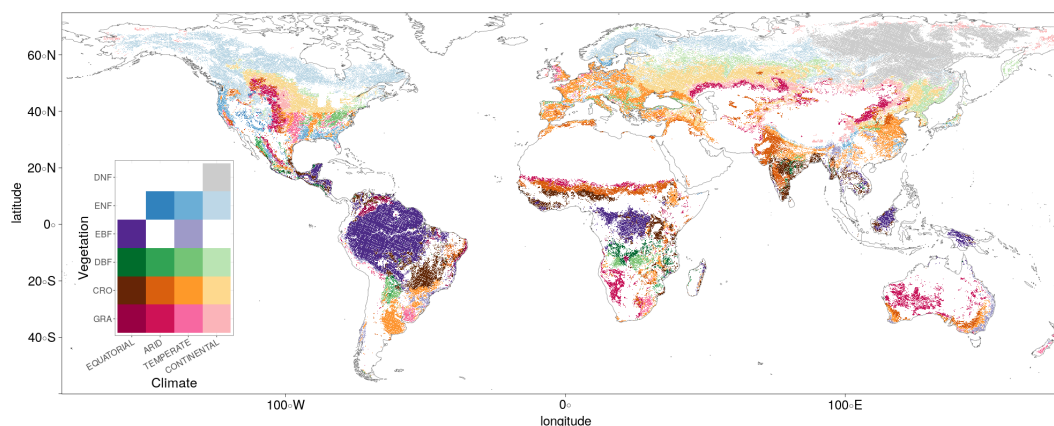

Figure 1. The dominant Köppen–Geiger climate zone and vegetation cover corresponding to each of the pixels passing the full set of selection requirements.

2.3 Growing season data

The Vegetation Index and Phenology (VIP) global dataset from NASA's Making Earth System Data Records for Use in Research Environments (MEaSUREs) program is used to define the growing seasons at each grid cell for each year (Didan, 2016). The datasets are created using surface reflectance data from the MODIS instrument. This data provides a consistent NDVI and EVI measurement from which to characterise the vegetation phenology. The Vegetation Index and Phenology (VIP) Phenology NDVI (VIPPHEN) v004 dataset has a global spatial resolution of $0.05°$ and provides annual metrics on the start and length of the growing season for each pixel for the years 2000-2014.

Whilst correlation between SIF and GPP has been observed across all seasons, only the relationship between downscaled SIF and FLUXCOM GPP during the growing season of each pixel is considered in the present study (Magney et al., 2019;

Bowling et al., 2018). This removes the effect of winter periods, when there is little primary productivity and when the retrieval of SIF can be problematic at northern latitudes. Off-season, the relatively weak SIF signal and the quality requirements in the downscaling process result in a dataset with gaps. Including this data in the analysis would likely result in distorted conclusions regarding average downscaled SIF signals over the time period. Additionally, only the first growing season of each year is considered in regions with multiple growing seasons.

2.4 SIF data

Two SIF datasets are considered in this analysis, produced via the downscaling method detailed in references Duveiller and Cescatti (2016) and Duveiller et al. (2020). The two retrievals have a spectral wavelength around 740nm, and differ in the retrieval method for obtaining the input data from the GOME-2 satellite, the first product developed by Joiner et al. (2013), is referred to as SIFJJ in this document, whilst the second, developed by Köhler et al. (2015), is referred to as SIFPK. A correction factor to convert the instantaneous SIF to the daily average is applied to both datasets to ensure comparability with estimates at different acquisition times (Frankenberg et al., 2011b; Köhler et al., 2018a). The downscaling method calibrates these input retrievals via a light use efficiency model using high resolution biophysical variables from the MODIS (MOderate Resolution Imaging Spectroradiometer) instrument of the Terra and Aqua Satellites. The optimal combination of variables is identified in combination with OCO-2 data, and the downscaled dataset is found to have a high level high spatio-temporal agreement with observations from the TROPOMI mission.

The resulting downscaled SIFPK and SIFJJ products have a spatial resolution of $0.05°$ and a temporal separation of 8 days (with measurements averaged over a sliding window of 16 days). The datasets currently cover the timespan 2007-2017, with 46 measurements each year (with the exception of the 2007 SIF dataset, containing 44). ~~In contrast to the coarse resolution SIF, the~~ Duveiller et al. (2020) shows that the downscaled SIFJJ dataset is found to have a slightly higher level of agreement with the OCO-2 validation data than the ~~SIFPK dataset~~ downscaled SIFPK dataset and so is primarily used in this paper, and is henceforth referred to as 'downscaled SIF' (or SIF_{DS}). ~~The SIFJJ has a lower bias, but more noise than the SIFPK, and the application~~ The higher agreement likely results from the spatial smoothing step of the downscaling ~~algorithm smooths the result, resulting in a less noisy downscaled product.~~ process that benefited the noisier SIFJJ more than the SIFPK.

To ensure high quality in the data, and compatibility with the other datasets, several requirements are placed on each pixel in each year, further to the requirements detailed in Duveiller et al. (2020), Köhler et al. (2015), and Joiner et al. (2013). There must be at least 10 instances of valid SIF_{DS} observations of the pixel within the growing season with fewer than 40% of the expected number of SIF_{DS} missing or invalid. There must also be least six years of valid measurements satisfying the requirements between 2007-2014. The selections ensure that the SIF signal, which is relatively weak compared to background noise, and affected by cloud coverage, is representative of the growing season as a whole as well as excluding regions with short growing seasons that may be more susceptible to fluctuations from unusual weather conditions. Requiring multiple years of data passing the quality requirements enables the investigation of temporal trends, whilst also ensuring that the measurements are representative of each pixel.
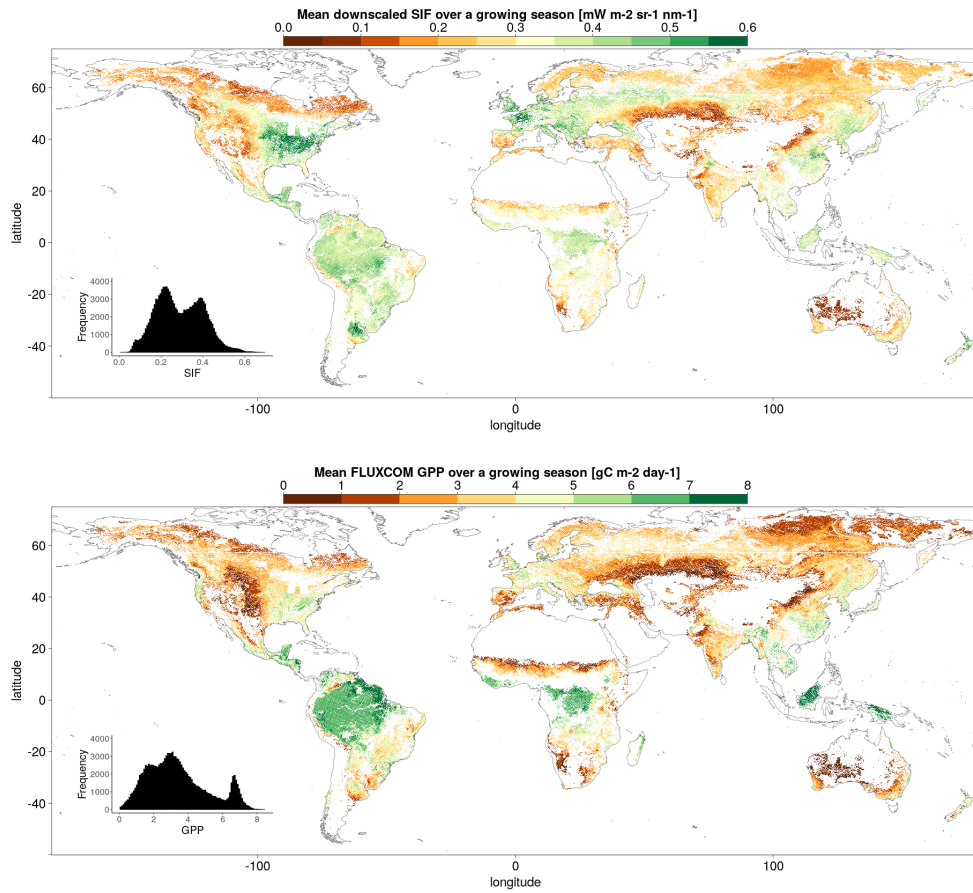
Figure 2. Mean downscaled SIF (above) and FLUXCOM GPP (below) over the growing season, corresponding to each of the pixels passing the full set of selection requirements. The SIF$_{DS}$ fluxes and GPP$_{FX}$ estimations for each pixel are averaged over multiple years between 2007 and 2014.

In order to reduce spatial auto-correlation and the double-counting of interpolated pixels in other datasets, pixels considered in the analysis must be separated by a two-pixel gap in all directions (Ploton et al., 2020). Each pixel is matched with the dominant vegetation cover and climate classification, as well as FLUXCOM GPP and meteorological data, passing the respective requirements. Figure 2 shows the mean downscaled SIF for the growing season of each pixel passing the analysis selection requirements, averaged over the period 2007-2014.

2.5 GPP data

The gross primary productivity (GPP) dataset is provided by the FLUXCOM project, measured as a daily carbon uptake [gC m^{-2} day^{-1}] (Jung and FLUXCOM Team, 2016; Tramontana et al., 2016; Jung et al., 2020). In the 'RS only' setup used in this analysis and described in Tramontana et al. (2016) and Jung et al. (2019), an ensemble of nine machine learning methods

merge carbon flux estimations from FLUXNET eddy covariance towers with remote sensing data taken or derived from the MODIS sensor to estimate gross primary productivity across the terrestrial surface. The remotely sensed data includes land surface temperature, fraction of absorbed photosynthetic active radiation, normalized difference vegetation index, normalized difference water index and land surface water index. The resulting dataset, hereon referred to as 'FLUXCOM GPP' (or GPP_{FX}), consists of a global estimate of GPP at a spatial resolution of $0.0833°$. These estimates occur in timesteps of 8 days (46 over the course of a year) and cover the downscaled SIF data collection period up until the year 2016.

The GPP pixels are extrapolated via binomial interpolation to $0.05°$ pixels in order to focus on the comparison with the SIF_{DS} pixels. Figure 2 shows the FLUXCOM GPP for the growing season of each pixel passing the analysis selection requirements, averaged over the period 2007-2014.

2.6 Meteorological data

ERA5 is the fifth generation ECMWF reanalysis global climate and weather dataset, and the ERA5-Land dataset replays the land component of the reanalysis to provide land variables at an enhanced resolution at $0.1°$. The dataset is extrapolated via binomial interpolation to $0.05°$ pixels in order to focus on the comparison with the SIF_{DS} pixels, with only non-consecutive months considered, in order to reduce temporal autocorrelation.

Meteorological variables are obtained from the ERA5-Land monthly reanalysis dataset ~~(Muñoz Sabater et al., 2021; Muñoz Sabater, 201~~ (Muñoz Sabater, 2019b; Muñoz Sabater et al., 2021). These include: air temperature (t2m [°C]: temperature of air at 2m), surface net solar radiation (ssr [J m^{-2}]: amount of solar radiation reaching the surface of the Earth minus the amount reflected by the Earth's surface) and soil moisture (swvl1 [m^3 m^{-3}]: volume of water in soil layer 1, 0-7 cm, of the ECMWF Integrated Forecasting System). A variable that is not available is the mean monthly vapour pressure deficit (VPD [kPa]), the difference between the saturated vapour pressure and the actual vapour pressure (Grossiord et al., 2020). It is important in regulating the stomatal conductance of plants, and thus useful to relate to both SIF and GPP. Due to non-linearity in the vapour pressure-temperature response, the average saturated vapour pressure of each month is calculated from the average of the saturation vapour pressure at the mean daily maximum and mean daily minimum air temperatures over the course of the month, using the following formula (Allan and Pereira, 1998): ~~$e_s = [e°(T_{max}) + e°(T_{min})]/2$ where: $e°(T) = 0.061$x exp$^{17.27T/(T+237.3)}$~~

$$e_s = [e°(T_{max}) + e°(T_{min})]/2 \text{ where: } e°(T) = 0.061 \text{ x exp}^{17.27T/(T+237.3)} \tag{4}$$

The latter formula is also used in the calculation of the actual vapour pressure from the dewpoint temperature. The minimum and maximum air temperatures and the dewpoint temperature are taken from the ERA5-Land hourly reanalysis dataset (Muñoz Sabater, 2019a).

3 Methodology

The SIF_{DS}-GPP_{FX} spatio-temporal relationship at global scale is analysed via several diagnostics. Linear models and analysis of covariance (ANCOVA) are performed to determine the similarities and dissimilarities in the response across different vegetation

covers. Finally, the response of the SIF$_{DS}$ to fluctuations in meteorological conditions is investigated to assess the potential of this metric to diagnose the impact of environmental drivers. For the analysis, each $0.05°$ vegetated pixel is described by a time series of downscaled SIF, FLUXCOM GPP, and meteorological values, taken over the first growing season of each year between 2007 and 2014. This same set of 135,000 global pixels is used in each analysis of the current paper, with consideration given to the vegetation cover and climate zone of the pixels analysed.

Several sections of the analysis of the SIF-GPP spatio-temporal relationship are repeated with the alternative FluxSat GPP dataset (in place of the FLUXCOM GPP) and the TROPOMI SIF dataset (in place of the downscaled SIF) in order to ensure the robustness and consistency of the analysis. These can be found in appendix A3 and appendix A4 respectively.

3.1 The spatio-temporal relationship of SIF$_{DS}$ and GPP$_{FX}$

Since the processes and drivers of variability in SIF and GPP may differ in time and space, we designed an analytical framework to isolate the temporal components of the SIF$_{DS}$-GPP$_{FX}$ relationship at different temporal resolutions (intra-and inter-annual) from the spatial variations. The spatial component of the SIF$_{DS}$-GPP$_{FX}$ correlation is isolated by determining the multi-year mean SIF$_{DS}$ and mean GPP$_{FX}$ for each pixel. Here 'mean' refers to the mean daily value of the downscaled SIF or FLUXCOM GPP over the first growing season. These values are converted to a multi-year means by averaging over the period 2007-2014. The Pearson's spatial correlation coefficient, r, ~~is~~ and a least-squares linear model are calculated at both a global scale, as well as over a local moving window of $2.5°$ for each climate-vegetation category, with the latter requiring at least 10 pixels within the moving window to be assessed and reported. The temporal component of the SIF$_{DS}$-GPP$_{FX}$ correlation and linear model is assessed at both the inter- and intra-annual scales. The inter-annual correlation, refers to the temporal relationship between the mean growing season SIF$_{DS}$ and GPP$_{FX}$ values between consecutive years at the same location. It should be noted that a temporal degradation in the GOME-2 instruments has been observed, potentially affecting the long-term analysis of SIF trends and therefore the SIF-GPP relationship, particularly from 2015 onwards (Zhang et al., 2018b). Whilst this may have a slight impact on the analysis presented here - which uses data collected up until 2014 - we nevertheless consider the inter-annual comparison of SIF$_{DS}$ and GPP$_{FX}$ worthwhile. Meanwhile, the intra-annual correlation refers to the relationship between individual SIF$_{DS}$ and GPP$_{FX}$ values made at 8-day timesteps within a growing season, in order to determine the internal growing season statistics. ~~The correlation~~ A minimum of 10 observations within a growing season over at least 6 years is required. The correlation and slope parameter of the least-squares linear relationship at each pixel is calculated for each year considered and averaged over the multi-year time period.

3.2 The spatial linear relationship between SIF$_{DS}$ and GPP$_{FX}$

The same process and data used to isolate and determine the spatial component of the correlation is used to determine the global spatial linear relationships between SIF$_{DS}$ and GPP$_{FX}$. For this purpose, an area-weighted least squares linear model fits the global SIF$_{DS}$-GPP$_{FX}$ distribution of pixels for each climate and vegetation cover. Whilst theoretically the leaf photosynthesis may be zero when the quantity of emitted SIF radiation is zero, this does not necessarily imply that the canopy level SIF-GPP relationship extends linearly to zero, as the canopy level SIF-GPP relationship smooths over known non-linearities at finer

scales and lower SIF yields (Magney et al., 2020). Additionally, forcing the linear regression through the origin based on a prior expectation (in this case that SIF and GPP are simultaneously zero) that lies outside the bounds of the considered data will introduce a bias into the regression parameters. Therefore the intercept of the SIF_{DS}-GPP_{FX} relationship is not forced through zero to account for this variation, as well as potential deviations from linearity in the sampled pixels.

3.3 Spatial analysis of covariance between SIF_{DS} and GPP_{FX}

In order to assess and test similarities in the global SIF_{DS}-GPP_{FX} response between vegetation covers, an ANCOVA (analysis of covariance) is performed. ANCOVA compares linear regressions between two or more groups whilst controlling for a covariate to test about the stastistical significance of the effects. In this specific case, the downscaled SIF covariate is controlled for in a spatial linear regression with the FLUXCOM GPP that differes between vegetation and climate groups. A comparison of the regression slope and intercept between pairs of vegetation cover groupings is conducted in terms of the significance (through the p-value) and the size of the effect (through η^2). The p-value for the slope parameter is the probability of obtaining an equal or more extreme difference in the regression slopes of two vegetation groups under the null hypothesis that the vegetation cover has no effect. The p-value for the intercept additionally assumes the null hypothesis for the regression slope. The size of the effect is measured through η^2 ($0 \leq \eta^2 \leq 1$), the proportion of the sum of squares from the nominal grouping of vegetation cover, SS_{veg}, to the overall sum of squares for the linear relationship, SS_{lm}: $\eta^2 = SS_{veg}/SS_{lm}$

$$\eta^2 = SS_{veg}/SS_{lm} \tag{5}$$

Therefore, η^2 gives the proportion of the variance attributable to the vegetation cover grouping and is conceptually similar to the significance of the coefficient of determination, r^2, in linear relationships. Therefore the The p-value provides evidence for whether the difference in SIF_{DS}-GPP_{FX} response is significant between vegetation covers, and η^2 can be thought of as the magnitude of that difference. For each climate grouping, pairwise ANCOVA comparisons are made between vegetation covers for a sample of 400-1000 pixels.

3.4 Estimating global GPP with downscaled SIF

The derived global spatial linear SIF_{DS}-GPP_{FX} relationships are used to project the downscaled FLUXCOM GOME-2 SIF into an estimate of gross primary productivity, GPP_{Est}. This is also interpreted in terms of absolute and percentage differences to the FLUXCOM GPP, with the percentage difference calculated as: $GPP_{diff} = 100 \times (GPP_{Est} - GPP_{FX})/GPP_{FX}$

$$GPP_{diff} = 100 \times (GPP_{Est} - GPP_{FX})/GPP_{FX} \tag{6}$$

Mapping the differences between FLUXCOM GPP and GPP_{Est}, estimated using the downscaled SIF and SIF_{DS}-GPP_{FX} relationships, enables the display of areas where the global, category-dependent, linear relationships succeed or fail in replicating the GPP_{FX} from the local SIF_{DS} observations. There are three four different groupings of global linear relationships used in the breakdown. Firstly the GPP estimate depends only on separate SIF_{DS}-GPP_{FX} relationships for each Köppen–Geiger climate zone; secondly, the GPP estimate depends is carried out separately for each vegetation cover, with no consideration for the

climate zone; third, both the climate zone and vegetation cover are taken into account; and finally the groupings used are sug-
gested from the analysis of covariance. The latter is also used to display an estimate of global GPP based on the downscaled
SIF, scaled by the FLUXCOM GPP relationships.

3.5 The SIF$_{DS}$ response to meteorological fluctuations

~~In order to explore the potential capabilities of SIF as an early indicator of stress across different type of vegetation type, the response of~~ The response of length-of-day corrected downscaled SIF to anomalies in a number of meteorological variables
is analysed ~~. A specific~~ in order to determine similarities in response between different vegetation covers and to understand
the driving meteorological factors for SIF fluctuations in different climate zones. A focus is given to meteorological extremes,
investigated through the z-score from the long-term monthly mean~~, in order to determine what are the driving meteorological
factors for SIF fluctuations in different climate zones~~. The study uses the same initial data as the investigation into SIF$_{DS}$-GPP$_{FX}$
response, however monthly averages of the SIF$_{DS}$ are taken in order to compare with the month-averaged meteorological
variables. The meteorological factors considered are air temperature, solar radiation, soil moisture and vapour pressure deficit.
Additionally, only non-consecutive months within a growing season are included, in order to reduce temporal autocorrelation.

For every pixel, the mean and standard deviation of the SIF$_{DS}$ and meteorological variables is calculated for each month
over the period 2007-2014. These individual monthly values are re-expressed as a z-score for each pixel - i.e. the difference to
the 2007-2014 monthly mean, standardised by the standard deviation. ~~For comparative purposes, the~~ The FLUXCOM GPP is
also included ~~, however it should be notedthat the~~ in the analysis, though, as noted, the FLUXCOM GPP product takes several
remotely-sensed climatic variables as input ~~to the machine learning method, including land surface temperature, fraction of
absorbed photosynthetic active radiation, normalized difference water index and land surface water index, and therefore it is
not fully~~ and so is not independent of the meteorological ~~factors, unlike the downscaled SIF~~ drivers. The inclusion of the
GPP product enables a comparison with the SIF$_{DS}$, giving insight into whether the SIF behaves as may be expected of an
independent proxy for GPP.

4 Results

4.1 The spatio-temporal correlation of SIF$_{DS}$ and GPP$_{FX}$

The Pearson's correlation coefficient, r, between the downscaled SIF and FLUXCOM GPP is projected into figure 3, to display
areas of high and low temporal and local spatial correlation, along with the slope parameter of a least-squares linear model
between the two. Meanwhile, figure 4 displays the global spatial and average global temporal correlations for each vegetation
cover and climate zone for comparative purposes.

The first thing to note is that at a global scale, prior to the breakdown into separate climate-vegetation cover categories, there
is a reasonably strong correlation between the downscaled SIF and the FLUXCOM GPP. Between different climate-vegetation
groupings, however, there is variety in the strength of the correlation. Whilst the breakdown of the relationship by either climate
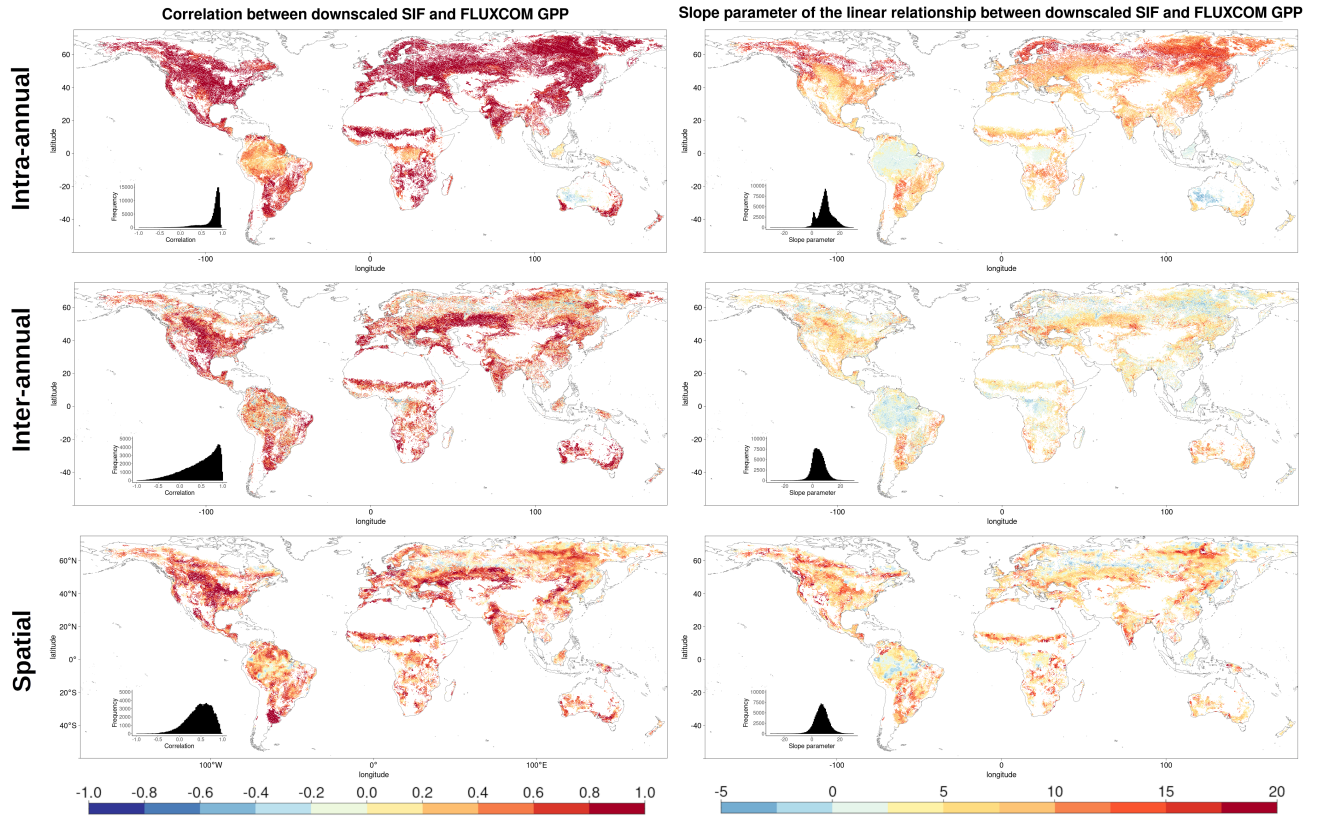
Figure 3. The Pearson's correlation coefficient, r, (left) and the linear model slope parameter (right) for: Above: the intra-annual temporal relationship between the downscaled SIF and FLUXCOM GPP over 8-day timesteps within a growing season. Middle: the inter-annual temporal relationship between the mean annual downscaled SIF and mean annual FLUXCOM GPP. Below: the spatial relationship between the mean annual downscaled SIF and mean annual FLUXCOM GPP, with the correlation determined for a given dominant vegetation cover and climate zone over a $2.5°$ moving window.
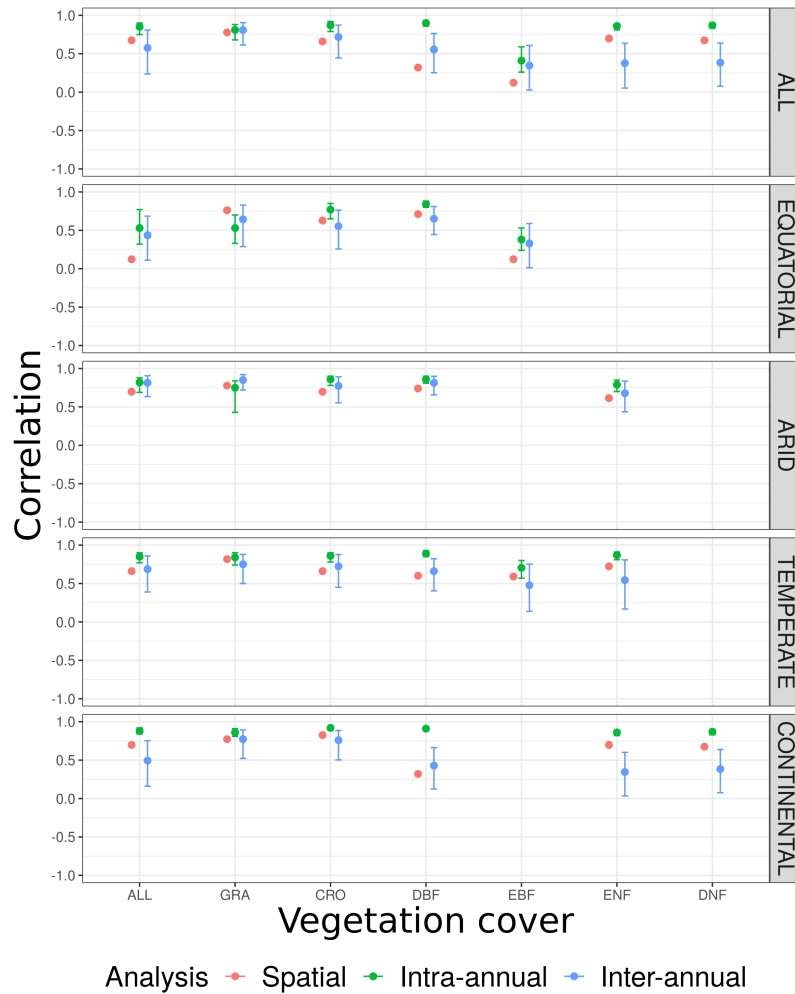
Figure 4. The Pearson's correlation coefficient, r, between downscaled SIF and FLUXCOM GPP for the spatial relationship, intra-annual temporal relationship within a growing season, and the inter-annual temporal trend across years. For the spatial analysis, a single global spatial correlation is calculated for each vegetation cover and climate zone, whilst the temporal relationships display the median global correlation and 25% upper and lower quantiles for each pixel, broken down by vegetation cover and climate zone.

zone or vegetation cover separately provides extra information in comparison to no breakdown, greater variability is shown from a breakdown by both categories simultaneously, highlighting the value of the downscaled SIF dataset in assessing the relationship with GPP across vegetation categories in different climates. The slight variation in correlation across different vegetation covers suggests that, although there are more similarities than differences, there is value in breaking down the relationship by vegetation cover.

The spatial and temporal analyses show that downscaled SIF functions as a reasonable spatial and temporal proxy for GPP, across multiple timescales and vegetation covers. The figures show that regions and vegetation-climate categories with high

correlation in one spatio-temporal analysis generally show high correlation in another analysis, suggesting that spatial and temporal correlation in the SIF_{DS}-GPP_{FX} datasets are actually interlinked. The highest correlations are almost exclusively found between between SIF_{DS} and GPP_{FX} within the same growing season as a result of the strong effect of seasonality in the key environmental drivers of primary productivity, such as radiation, temperature and water availability. Indeed, all vegetation-climate categories except for equatorial broadleaf forests exhibit $r > 50\%$ $r > 0.5$, with all regions outside the tropics and the arid grasslands of central Australia showing high correlation. Larger intra-annual slope parameters between SIF_{DS} and GPP_{FX} are similarly found in the high latitude regions which experience the largest seasonality.

The spatial correlation and the temporal trend between years show similar features, though are generally weaker than the intra-annual correlation, with some regions of tropical rainforest and continental forest in Russia displaying anti-correlation. There is also a wider distribution in the strength of the SIF_{DS}-GPP_{FX} correlation. This is despite the fact that the temporal analyses have a more granular level of spatial detail, with each pixel more susceptible to fluctuations. This is particularly true of the inter-annual comparison, which uses fewer data points in the regression.

4.2   The spatial linear relationship between SIF_{DS} and GPP_{FX}

Figure 5 shows the relative distribution and spatial linear relationship between the mean growing season FLUXCOM GPP as a function of the respective mean values of the downscaled SIF during the growing season. The data are broken down into separate categories depending on the Köppen–Geiger climate grouping and dominant vegetation cover of the pixel.

The significant substructure in the SIF_{DS}-GPP_{FX} distribution and greater deviation from the linearity in the 'ALL' categories, give evidence to the fact suggest that the SIF_{DS}-GPP_{FX} spatial relationship response is dependent on both the climate and vegetation covers. There is also some evidence that there is a slight trend towards a reduction in the slope in cooler climates, though this may result from factors other than the climate itself, for example, differences in the spatial distribution of vegetation between evergreen and deciduous types or between C3 and C4 crops and grasses.

In all categories except EBF, the spatial correlations are comparable to the relationship observed between FLUXCOM GPP and SIF measurements from the OCO-2 instrument, as seen in Sun et al. (2018) confirming the overall value of the downscaled SIF product for this specific exercise. In this the Sun et al. (2018) study, the following correlation coefficients are exhibited (broken down by biome): $r_{GRA} = 0.74$; $r_{CRO} = 0.88$; $r_{EBF} = 0.74$; $r_{DBF} = 0.8$; $r_{NF} = 0.84$ (needleleaf). The differences to this study may result from the selection criteria of the biomes, the singular grouping of vegetation covers across different climate zones, and the forcing of the linear relationship intercept through zero. In particular, the latter assumption of the SIF-GPP relationship leads to higher correlation coefficients compared to the case when the intercept may allowing the intercept to float. The observed linear relationship is found to be stronger with the FluxSat GPP dataset, as displayed in appendix A3

We acknowledge that, in some categories, a linear model may be too simplistic to represent the relationship between SIF_{DS} and GPP_{FX}. This is more true for the woody plants which display some complexity in the SIF_{DS}-GPP_{FX} relationship, in contrast to herbaceaous vegetation, which remains highly linear, despite exhibiting a greater range in values. The clearest deviation from linearity is found in highly productive equatorial evergreen forests, where a wide range of spatio-temporal variation in SIF_{DS}
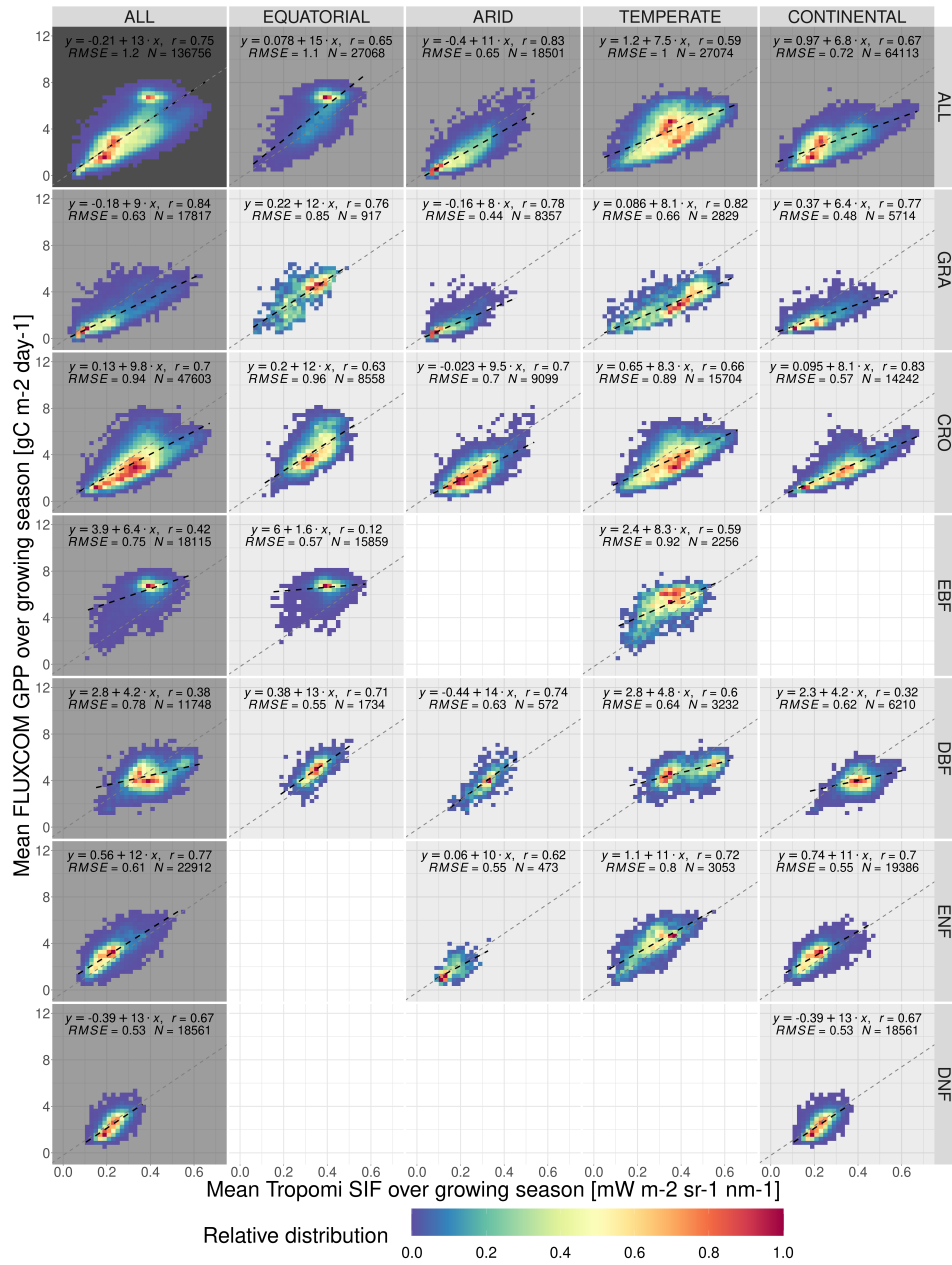
Figure 5. The spatial relationship between the mean growing season downscaled SIF and FLUXCOM GPP, broken down into separate Köppen–Geiger climate zones and vegetation cover categories. The plot shows the frequency distribution of pixels into SIF_{DS}-GPP_{FX} bins, relative to the highest frequency bin in that category. A black dashed line representing a linear model in each category is overlaid and compared to a grey dotted line representing a linear model produced without the breakdown into separate categories (i.e. 'ALL-ALL'). The linear model equation, correlation coefficient r, root mean squared error (RMSE) and number of pixels are included.

355   is observed, while a considerably smaller variability is reproduced in the modelled GPP$_{FX}$. This non-linearity is explored in more depth in the discussion.

    Whilst at first glance the heatmap of temperate deciduous broadleaf forests similarly hints at a plateau effect, the figure can in fact be divided into two areas of high SIF$_{DS}$ and low SIF$_{DS}$ data points corresponding to separate spatial locations. The lower SIF$_{DS}$ values correspond to deciduous forests in Southern Africa and South America, whilst the higher SIF$_{DS}$ values occur

360   in North America and Europe, suggesting that there may not be global universality in the SIF$_{DS}$-GPP$_{FX}$ relationship, or that different types of deciduous broadleaf forests found in distinct regions could respond differently, possibly based on differences in species composition. It should be noted that this distinction is not observed in the TROPOMI SIF dataset for the year 2020 (appendix A4).

4.3   Spatial analysis of covariance between SIF$_{DS}$ and GPP$_{FX}$

365   The results of the analysis of covariance between pairs of vegetation covers within a climate zone, are shown in ~~table ?? through the p-value and~~ figure 6 through the η^2 for the slope and intercept of the linear relationship. It should be noted that the ANCOVA analysis assumes linearity between SIF$_{DS}$ and GPP$_{FX}$, which is present in most vegetation covers, with noted exceptions. ~~In each climate category, vegetation cover pairs with the largest η^2 for the slope are listed first, where the slope is significant (p-value < 0.05). If differences in the regression slope are not significant (i.e. the slopes are considered to be~~

370   ~~parallel), then the difference in the size of the effect of the intercept is considered, such that the lowest ranked pairs within a climate zone are the most similar in their SIF$_{DS}$~~Appendix A1 contains the full table of results, whilst similar analyses comparing the downscaled SIF - ~~GPP$_{FX}$ response~~FluxSat GPP relationship and the TROPOMI SIF - FLUXCOM GPP relationship can be found in appendices A3 and A4 respectively.

    The ANCOVA results in equatorial regions show that the categorisation by vegetation class is not a significant factor in

375   the slope-dependence of the SIF$_{DS}$-GPP$_{FX}$ for all vegetation types except evergreen broadleaf forests, which, as discussed, exhibits non-linearity in the SIF$_{DS}$-GPP$_{FX}$ relationship. Differing intercepts between the DBF and the herbaceous vegetation covers, however, suggest that whilst the SIF$_{DS}$-GPP$_{FX}$ relationship scales in similar ways between vegetation covers, there may be differences in the starting potential. Linear relationships in grass and cropland are statistically indistinguishable, whilst around 10% of the sum of squares between DBF and CRO/GRA intercepts can be attributed to the vegetation classification.

380   In equatorial broadleaf forests $12-19\%$ of the difference in the SIF$_{DS}$-GPP$_{FX}$ scaling can be attributed to the categorisation, and therefore when using SIF as a proxy for productivity, EBF should clearly be considered separately from other vegetation classes.

    In arid climates the difference between the slopes of vegetation covers is significant in terms of the p-value for all except the ENF-CRO pair. However, there is little to distinguish the SIF$_{DS}$-GPP$_{FX}$ scaling by vegetation categories, with less than

385   2% of the sum of squares attributable to the vegetation covers for all except GRA-DBF (7%). If the assumption is made that the vegetation categorisation has no effect on the SIF$_{DS}$-GPP$_{FX}$ slope, and that the slopes can be considered parallel between vegetation covers, then the intercepts generally distinguish between the woody and non-woody vegetation covers, with crossover in CRO-ENF. Between the ENF-DBF intercepts, 2% of the sum of squares is attributable to the vegetation
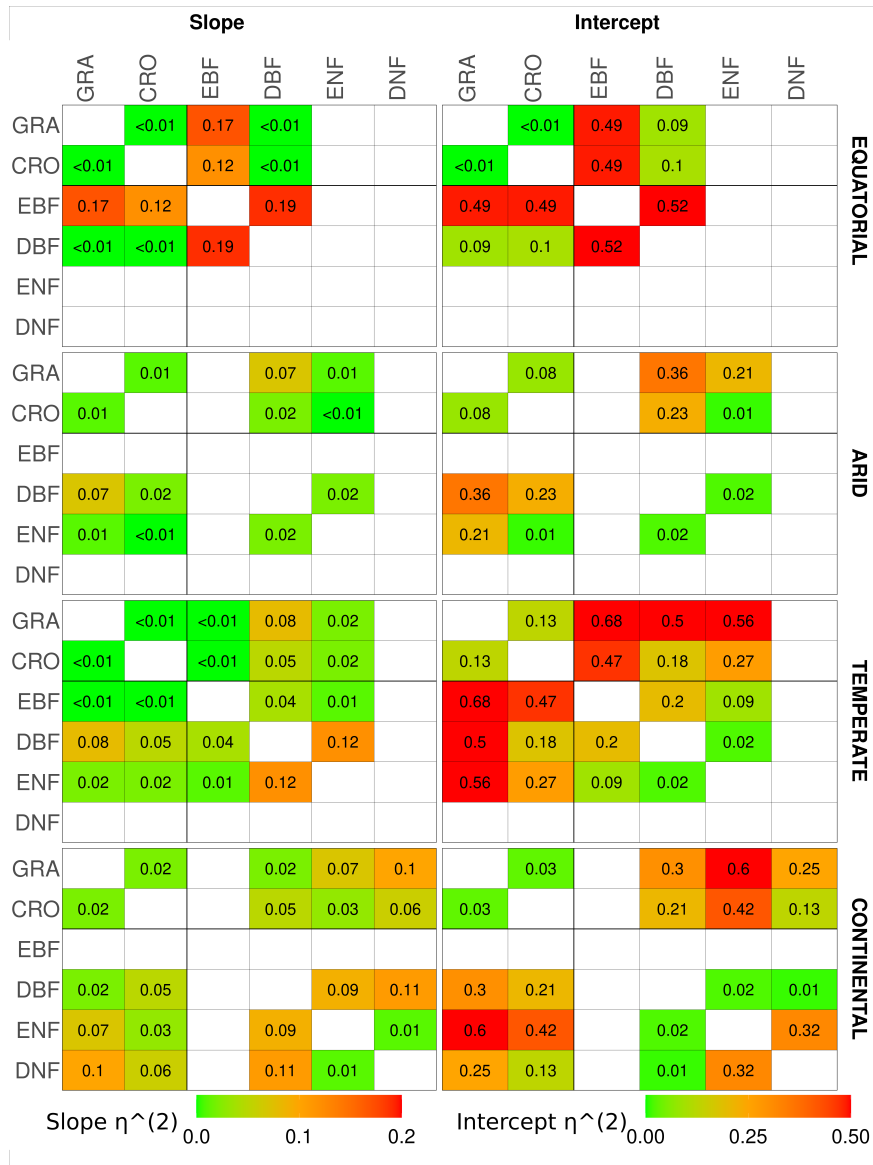
17

Figure 6. The η^2 parameter of an analysis of covariance between pairs of vegetation covers in different Köppen–Geiger climate groupings, for the slope (left) and intercept (right) of the linear relationship between downscaled SIF and FLUXCOM GPP. ANCOVA is performed on the intercept under the assumption that the difference between slopes is not significant. The η^2 parameter is comparable to the percentage of the difference in the slope or intercept (the latter assuming equivalence of the slopes) attributable to the difference in vegetation cover, with lower values signifying a smaller difference between vegetation covers. A slightly bolder line is used to separate the herbaceous species (CRO, GRA) from the woody species (EBF, DBF, ENF, DNF).

cover, whilst the proportion is 8% for GRA-CRO. Mixing between herbaceous and woody covers, on the other hand, and the proportion of the sum of squares attributable to the vegetation cover is between $21 - 36\%$, with the exception of ENF-CRO, which are statistically almost indistinguishable.

In temperate regions the only major distinction in the gradient of the SIF_{DS}-GPP_{FX} relationship between vegetation covers is found in deciduous broadleaf forests ($4 - 12\%$). As discussed in the previous section, temperate DBF is dominated by two distinct Northern and Southern hemisphere clusters with differing SIF_{DS}-GPP_{FX} relationships, which results in a distinct and separate linear relationship. This feature is not observed in the TROPOMI SIF analysis. Regarding the other vegetation covers, assuming that the categorisation is of little importance to the slope, accounting for $\leq 2\%$ of the sum of squares, and that the slopes could be considered parallel between the vegetation covers, the differences in the intercept broadly divide along the lines of woody and herbaceous species. The sum of squares attributable to differences in the intercept are: woody-woody, 9%; herbaceous-herbaceous, 13%; woody-herbaceous, 27-68%.

Finally, in continental climates, ENF and DNF species exhibit a similar ($< 1\%$) SIF_{DS}-GPP_{FX} scaling (though a much larger difference attributable to the intercept 30%) and are somewhat distinct from the other vegetation species ($6 - 11\%$), with the exception of CRO-ENF (3%). This feature in the slope of continental needleleaf forests is not observed in the analysis that uses FluxSat GPP in place of the FLUXCOM GPP. Within these other vegetation species, $< 5\%$ of the difference in the SIF_{DS}-GPP_{FX} slope can be attributed to the choice of vegetation cover and, assuming the null hypothesis for the slope, the intercept again distinguishes between the herbaceous plants (GRA-CRO, 3%) and mixed, herbaceous-woody (DBF-CRO, 21%; DBF-GRA, 30%).

Overall, ~~the~~ when analysing the the scaling of the SIF_{DS}-GPP_{FX} response (i.e. the slope) between vegetation covers within a climate zone, the ANCOVA analysis suggests that there ~~is a~~ are large similarities, with potential slight exceptions in temperate deciduous broadleaf forests, continental needleaf forests, and the major exception of tropical evergreen forests. In terms of the scaling of the SIF_{DS}-GPP_{FX} slope, these three vegetation covers may be treated as being reasonably distinct, with at least around 5% and up to 20% of the difference between slopes being attributable to the vegetation classification. Amongst the other species where the slope does not distinguish between vegetation covers so prominently (with generally less than 3% of the slope variation attributable to the vegetation categorisation), the intercept, and therefore the systemic difference between the linear relationships, loosely depends on whether the species is woody or herbaceous, with higher values for woody species. The difference in the SIF_{DS}-GPP_{FX} response between cropland and grassland is particularly minor. A caveat must be made that there are some exceptions to these generalisations, and there is no statistically concrete global distinction between groupings of vegetation covers.

The results demonstrate that within a climate grouping there are broad similarities in the SIF_{DS}-GPP_{FX} response of the considered vegetation classifications, excluding three key exceptions. When accounting for differences in the intercept, a loose possible grouping may be suggested of herbaceous and woody vegetation within each climate zones, with the exceptions of equatorial-EBF, temperate DBF, and continental forests (which can be fully distinguished when the difference in the intercept is considered, or split between broadleaf and needleleaf if considering only the scaling). This reduces the climate-vegetation

categories for which we expect differing SIF_{DS}-GPP_{FX} responses from 18 groups to 12 overall, with around three distinct groups in each climate zone, depending on the aggressiveness of the grouping.

4.4 Estimating the global spatial distribution of GPP with downscaled SIF

The mean growing season downscaled SIF can be projected into an estimate of growing season GPP using the global linear relationships for each climate and vegetation cover category displayed in figure 5. The absolute and percentage difference of this estimated GPP, GPP_{Est}, to the FLUXCOM GPP is shown in figure 7, which displays areas where the global, category-dependent, linear relationship shows positive or negative biases in replicating the GPP_{FX} from the local SIF_{DS} observations. The figures are created using three different versions of the global spatial linear relationships between SIF_{DS} and GPP_{FX}. In the first instance, four separate linear relationships are derived for the four different climate zones. In the second instance the linear relationships are derived separately for each climate zone and vegetation cover, with 18 separate SIF_{DS}-GPP_{FX} relationships. Finally, separate linear relationships are derived in each climate zone for each the different vegetation groupings suggested by the results of the analysis of covariance, with 12 groups overall.

The figures show that there is added value for GPP prediction in breaking down the relationship into the differing vegetation covers since the ~~SIF-GPP~~ SIF_{DS}-GPP_{FX} relationship is not climate and vegetation invariant. When only the Köppen–Geiger climate grouping is used to classify the spatial SIF_{DS}-GPP_{FX} relationships, there is a significantly greater difference between the FLUXCOM GPP and the GPP estimated from the downscaled SIF, compared to when vegetation cover is taken into account. As may be expected, the vegetation covers flagged as particularly distinguished in their spatio-temporal SIF_{DS}-GPP_{FX} response, such as equatorial evergreen forests and continental needleleaf forests, especially suffer from this lack of a breakdown. When only the vegetation covers are considered, and no climate grouping is proposed, there is a smaller difference between the estimated GPP and the FLUXCOM GPP than in the case of the climate groupings alone, suggesting that differences between vegetation covers are more important in determining the SIF_{DS}-GPP_{FX} relationship than the climate zone grouping. However there are still noticeable differences compared to the relationships that include a breakdown by climate grouping, as can be seen in the width of the inset histograms. The similarity in the lower figures, where the SIF_{DS}-GPP_{FX} scaling depends on the grouping suggested by the analysis of covariance, compared to the unique vegetation covers in the middle figures, show that whilst vegetation cover appears to be an important parameter in classifying SIF_{DS}-GPP_{FX} relationships, it is possible to combine vegetation groups in a way that doesn't noticeably affect the SIF_{DS}-GPP_{FX} scaling. It should be noted that vegetation cover here may be a proxy for other variables, such as local conditions, soil type or a refined climate grouping, and in this sense further investigation in similar, localised conditions is required.

Figure 8 shows the global gross primary production estimated from the downscaled SIF and the SIF_{DS}-GPP_{FX} relationships between vegetation groupings suggested by the ANCOVA results. It is particularly notable that in equatorial rainforests, the flat linear relationship derived between SIF_{DS}-GPP_{FX} results in estimated GPP values with low variation.
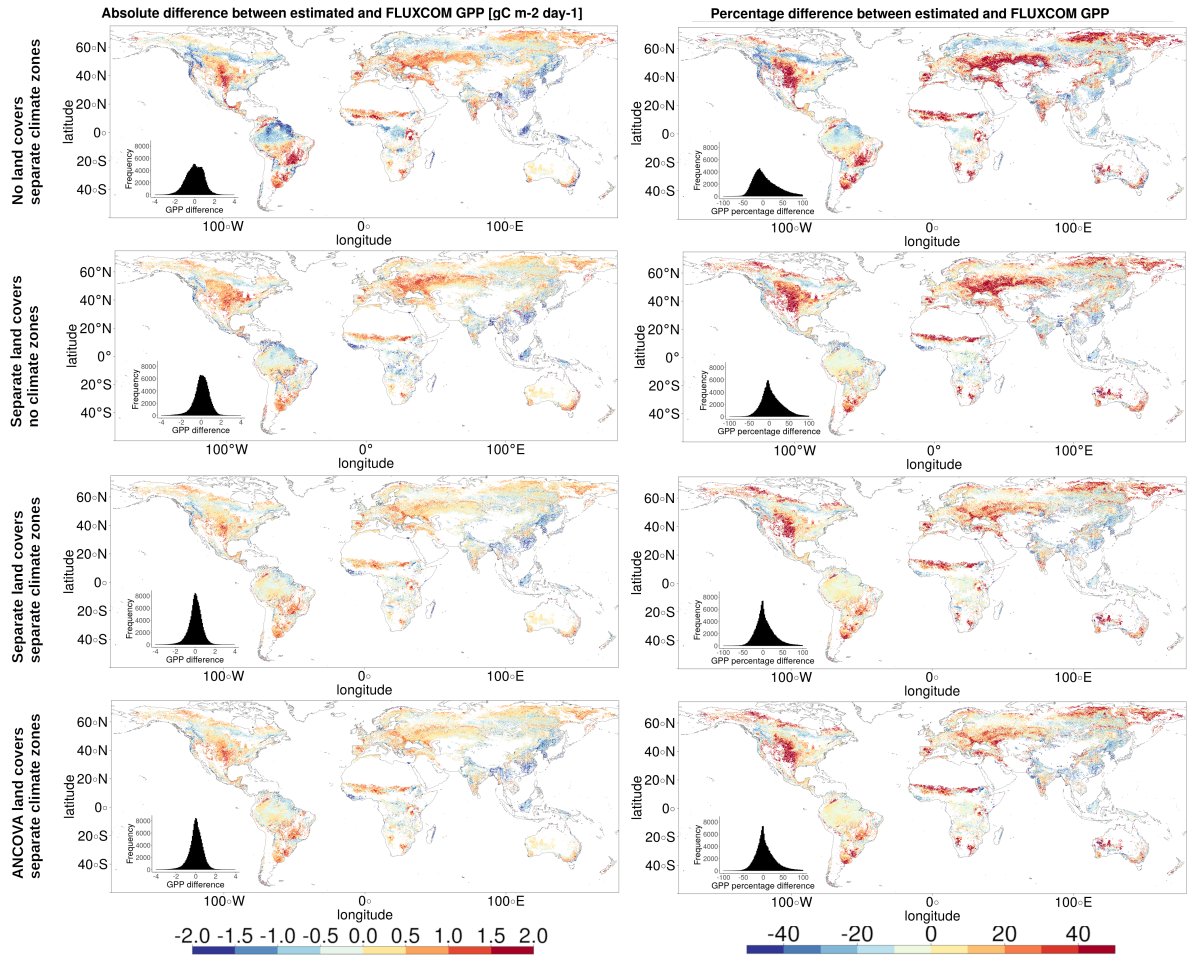
Figure 7. The absolute (left) and percentage (right) difference between the mean annual estimated primary production, GPP_{Est} and the mean annual FLUXCOM GPP. GPP_{Est} is estimated by projecting the downscaled SIF at each pixel using SIF_{DS}-GPP_{FX} relationships derived within: top, each climate zone; upper middle, each vegetation cover; lower middle, each vegetation cover within each climate zone; bottom, different climate-vegetation groupings suggested by the analysis of covariance.

4.5 The SIF_{DS} response to meteorological fluctuations

455 Figure 9 shows the average z-score of the SIF_{DS} with respect to the z-score of the four meteorological variables considered in this study as environmental drivers of primary productivity. Each bin contains multiple data points (at least five in order to be displayed) with the SIF_{DS} z-score taken as the average of the data points within the bin. The figure shows how anomalies in monthly values of climate drivers - relative to the 'average' conditions for that month - are related to fluctuations in SIF_{DS}. The figures are broken down into the same categorisation as in the previous study, clearly showing that in the various climates,

460 vegetation covers respond differently, and sometimes in opposing directions, to climate drivers depending on the limiting
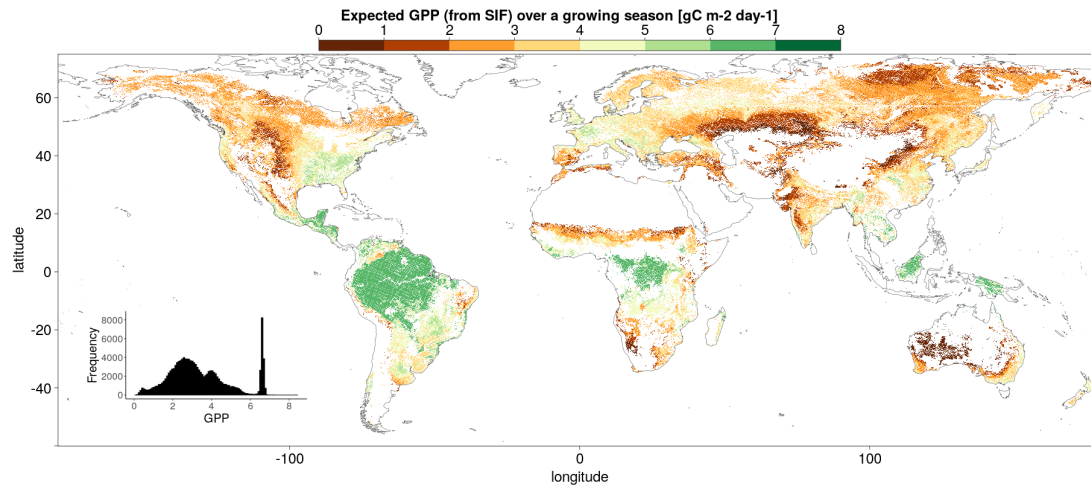
Figure 8. The global GPP estimated from the downscaled SIF and the SIF_{DS}-GPP_{FX} spatial linear relationships between vegetation groupings suggested from the results of the analysis of covariance.

factor of photosynthesis (e.g. water scarcity, low temperatures, etc). Equivalent figures for the FLUXCOM GPP can be found in appendix A2.

Figure 10 shows the average SIF_{DS} and GPP_{FX} z-scores as a function of the corresponding z-score of the four meteorological variables. The figure uses the exact data that is input into figure 9, and categorises the temperature, VPD, soil moisture and solar radiation z-score of pixels from the long-term monthly mean into 10 groups between -2.5 and +2.5. The median corresponding SIF_{DS} and GPP_{FX} z-scores, relative to the long-term monthly mean of each pixel, are shown for each meteorological variable. The results are broken down by the Köppen–Geiger climate and vegetation cover groupings discussed previously. The figure therefore shows the average SIF_{DS} and GPP_{FX} fluctuations that correspond to a given fluctuation in each meteorological condition, and can be used to interpret the meteorological drivers that may result in fluctuations in vegetation productivity.

The first point to note is that the link between SIF_{DS} and meteorological fluctuations is more significant in some climate/vegetation cover categories than others. The SIF_{DS} from grasslands and croplands responds in a very similar manner across all climates, but often differs from the response of woody vegetation. The SIF_{DS} and GPP_{FX} together respond in a similar way to the meteorological fluctuations, with the GPP_{FX} generally more responsive, particularly in the case of woody vegetation. This is likely caused by the inclusion of meteorological information in the FLUXCOM GPP product, resulting in a correlation and so over-sensitivity. Whilst the SIF_{DS} may be less sensitive in general, unlike the FLUXCOM model it also captures information relating to the physiology of the plant, potentially bringing extra information into consideration when determining vegetation response.

Clear and expected trends in the SIF_{DS} data can be picked out. For example, plants in cooler climates respond more positively to higher temperature fluctuations and plants in arid climates benefit significantly from soil moisture and reduced VPD (more humid conditions). Arid and continental climates, which in general are often harsher environments for plant life, exhibit a larger
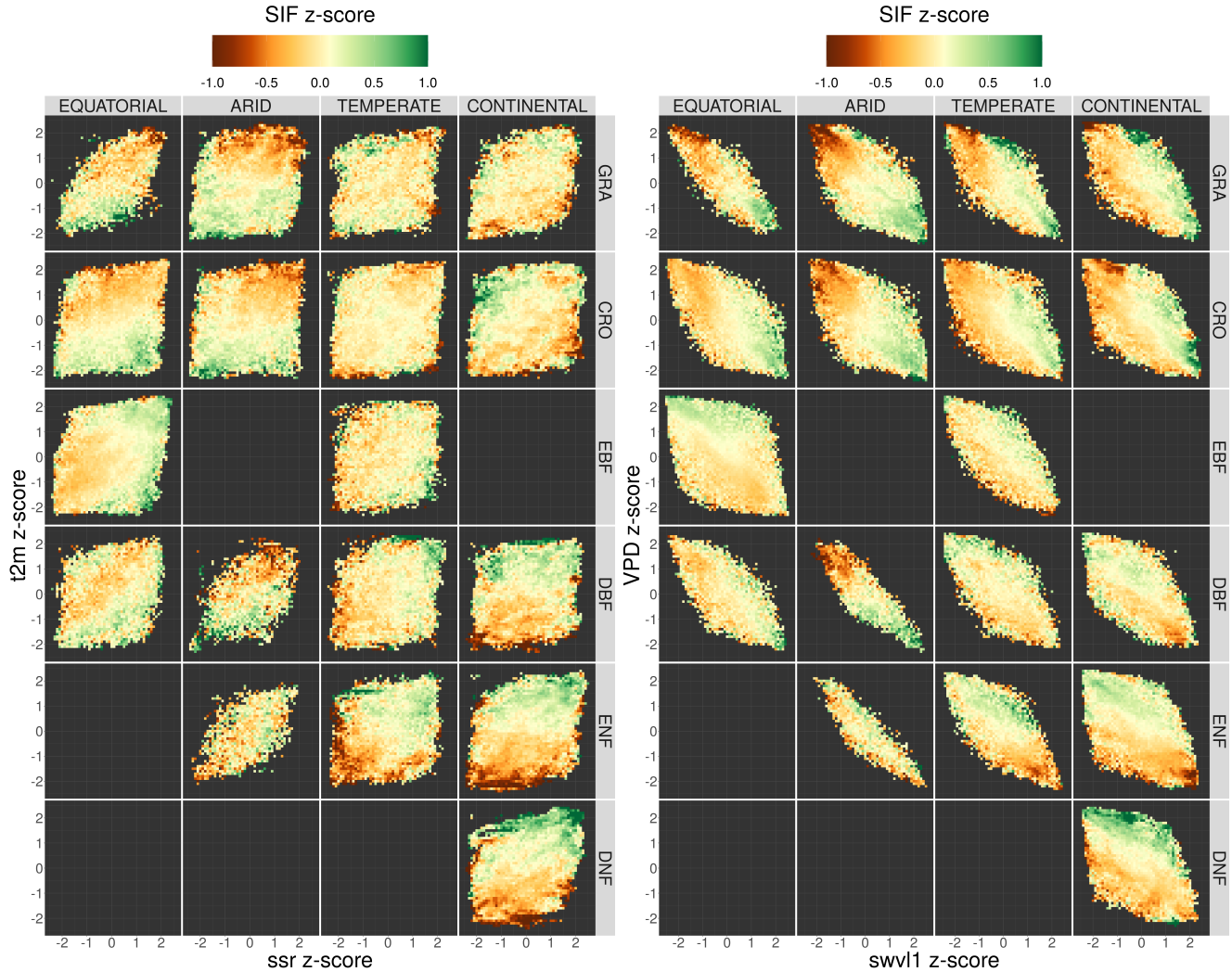
Figure 9. The relationship between fluctuations in meteorological variables and the corresponding fluctuations in the measured downscaled SIF. The fluctuations are measured relative to the monthly mean for each pixel and expressed as a z-score. The four meteorological variables are air temperature and net surface solar radiation (t2m and ssr, left) and vapour pressure deficit and soil moisture (VPD and swvl1, right). The SIF$_{DS}$ response in each bin is the mean of all data points in each bin of meteorological z-score. The data is broken down into separate Köppen–Geiger climate zones and land cover categories.

meteorological dependence than equatorial and temperate ones, whilst herbaceous plants are generally also more weather dependent. As the SIF$_{DS}$ response is measured with respect to conditions in an average month, the response often differs between Köppen–Geiger climates, for example, DBF and ENF forests respond positively to VPD (drier air) in temperate and continental climates but negatively in tropical and arid climates.
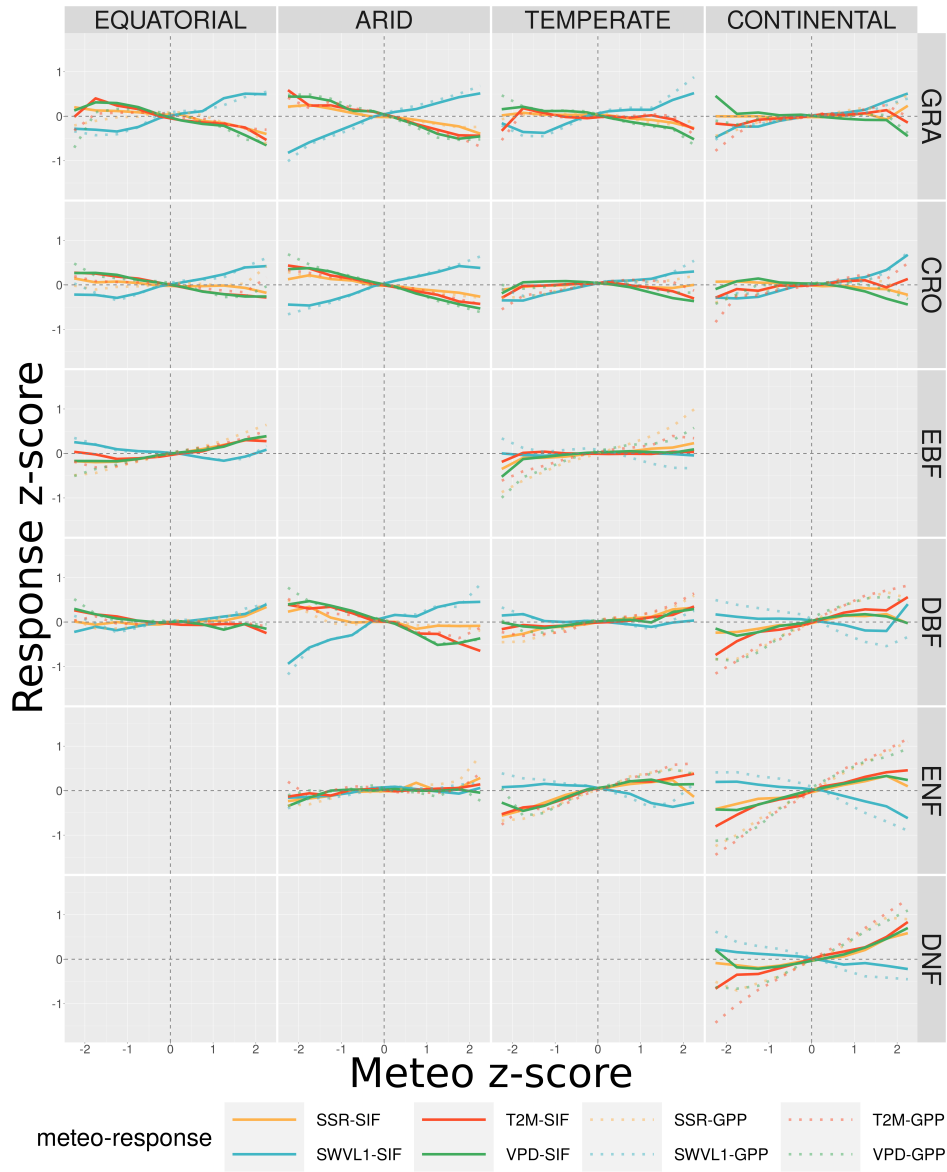
Figure 10. The average fluctuation in the remotely-sensed downscaled SIF and FLUXCOM GPP, as a function of the fluctuation in several meteorological variables. The fluctuations are defined in terms of the z-score of each variable, calculated for 10 different bins between -2.5 and 2.5, and the corresponding median SIF_{DS}/GPP_{FX} z-score, relative to the long-term (2007-2014) monthly mean for each pixel (each pixel may contribute multiple months within the growing season). The meteorological variables considered from the Copernicus Climate Service (C3S) Climate Data Store (CDS) and are: surface net solar radiation (SSR), air temperature (T2M), vapour pressure deficit (VPD) and soil moisture (SWVL1). The data is broken down into separate Köppen–Geiger climate zones and land cover categories.

The response of SIF$_{DS}$ to fluctuations in the meteorological variables is not always of simple interpretation since there may be co-limitation from multiple drivers linked by complex correlation patterns. In figure 9, co-limitation is observed where the direction of the SIF$_{DS}$ response lies along the diagonal, for example the preference for both high temperatures and high levels of radiation in temperate deciduous broadleaf forests, or for ~~condition~~ conditions of low VPD and high soil moisture content in grassland and croplands. ~~Strong correlation is noticeable in the SIF$_{DS}$ response to meteorological fluctuations, as~~ ~~can be seen clearly in equatorial rainforests in figure 10: high VPD correlates with high cloud cover, limiting the solar radiation~~ ~~arriving at the leaves and, naturally, reducing temperatures and affecting rainfall (and therefore soil moisture). Meanwhile,~~ Co-dependence between the atmospheric variables means that it is difficult to directly explain fluctuations in SIF$_{DS}$ via individual meteorological variables in isolation of the other meteorological variables, for example, the correlation between warmer temperatures and high VPD, results in a similar SIF$_{DS}$ response in cooler continental woody forests. Additionally, differences and sub-patterns in the SIF$_{DS}$-meteorological response may be complicated by the spatial distribution of plant species, which is not captured by the broad Köppen–Geiger categorisation. For example equatorial EBF forests may be located in wetter environments than Equatorial DBF forests, and therefore profit from differing fluctuations in the local climate, in this case a lower soil moisture and higher VPD.

Figure 10 shows that the strength of the relationship between the SIF$_{DS}$ fluctuations and the meteorological fluctuations generally increases for more extreme deviations of SIF$_{DS}$. For example, in continental deciduous needleleaf forests, a two standard deviation increase in the temperature (relative to the long-term mean for that month) corresponds to a SIF$_{DS}$ that is an average of 0.8 standard deviations higher than usual. In comparison, a smaller temperature fluctuation of between 1 and 1.5 standard deviations above the monthly mean temperature would correspond to a slightly lower increase in the SIF (+0.3 standard devations above the monthly mean). The results therefore provide evidence that not only do fluctuations in meteorological conditions correspond to fluctuations in SIF, but more extreme fluctuations often result in more extreme fluctuations in SIF. In this context the study suggests that it ~~is~~ may be possible to use high-resolution SIF as a near-real time measure of ~~the~~ ~~resilience of ecosystems to climate~~ the response of vegetation productivity to climate fluctuations, as well as demonstrating where vegetation may be resistant to certain fluctuations. For example, evergreen broadleaf forests appear to show relatively little deviation in SIF up to reasonably extreme weather fluctuations. It is important to note though, that 'extreme fluctuations' here are measured relative to a location's average climate variation, which may be small in absolute terms compared to other categories. As the climate categorisation considered in this study is relatively broad, further research of using high resolution SIF on specific ecosystems is required.

Finally, the results are used to determine the driving and limiting climate variables on a global scale. Figure 11 shows a map of the meteorological variable corresponding to the highest and lowest average SIF fluctuation.
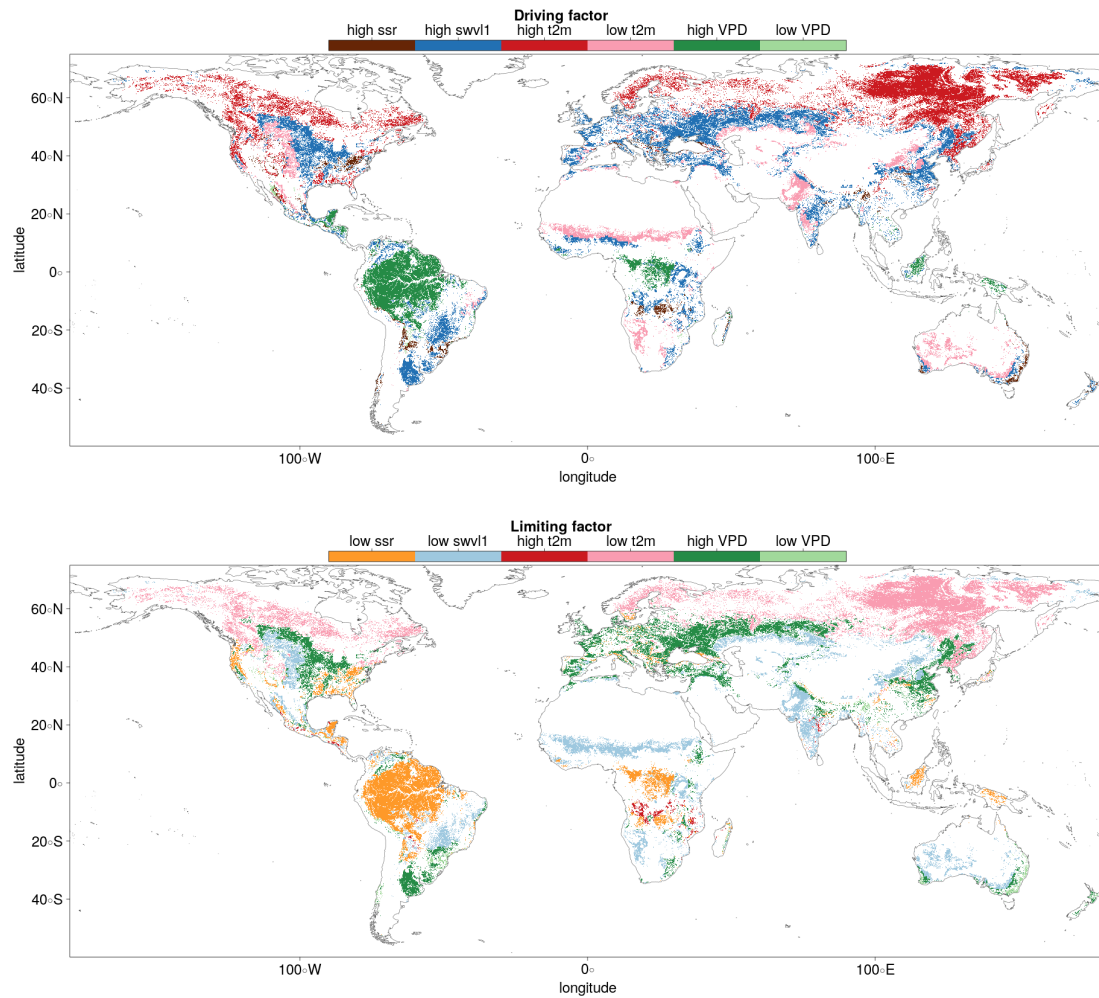
Figure 11. The driving (above) and limiting (below) meteorological conditions displayed at a globe scale. The driving and limiting variables are those that respectively correspond to the largest upward and downward fluctuations in downscaled SIF for each Köppen–Geiger climate-vegetation grouping.

5 Discussion

5.1 The use of downscaled SIF be used as a proxy for GPP: does it add value?

The study demonstrates the utility of the Duveiller et al. (2020) downscaling method in providing a robust, high-resolution SIF dataset that can be used as proxy for gross primary production. This method uses a light-use efficiency modelling based approach to establish a relationship between SIF and higher resolution remote sensing variables. The resulting high resolution SIF_{DS} benefits the analysis in enabling higher ~~purity~~ quality selections in the vegetation classification of pixels, and therefore more precision when assessing the different dynamics and patterns of the relationships between SIF_{DS} and GPP_{FX} across

26

different vegetation covers and climate regions. A high level of spatio-temporal correlation is found across almost all Köppen–Geiger climate and vegetation groupings, comparable to levels observed between non-downscaled SIF and FLUXCOM GPP. Breaking down the correlations into their separate constituent vegetation covers shows diversity in the SIF_{DS}-GPP_{FX} relationship, and therefore that there is some dependence on vegetation cover in the relationship between canopy-level SIF and vegetation productivity. For the most part, the downscaled SIF reproduces the spatial patterns observed in the FLUXCOM GPP data, for example in figure 2, and scales linearly, with a few notable exceptions.

The clear response of SIF_{DS} to meteorological fluctuations of key climatic drivers shows that it is possible to observe the temporal patterns and anomalies of vegetation productivity and stress remotely, via satellite. This suggests the possibility of using SIF in the near-real-time monitoring of vegetation ~~stress in~~ reaction to environmental conditions. As climates change it becomes increasingly important to know how vegetation responds to both long-term trends in the climate as well as increasingly frequent extreme weather events.

The reproduction of known SIF-GPP patterns using the downscaled SIF demonstrates its utility as a high-resolution proxy of primary productivity. In support of these conclusions, appendix A4 replicates the main analysis results with the substitution of a single year of TROPOMI data in place of the downscaled SIF, whilst appendix A3 ensures the conclusions are not unique to the choice of the GPP dataset. In this sense the analysis serves as a diagnostic benchmark for the comparison of SIF and GPP datasets. The use of the downscaling method on recent and future retrievals of SIF, such as the high-resolution retrievals from the TROPOMI satellite instrument, will enable further study on the relationship between SIF and GPP. Furthermore, the current downscaled SIF dataset provides an archive at a comparable resolution for the analysis of trends across longer timescales.

5.2 Areas of divergence between SIF_{DS} and GPP_{FX}

Figure 2 shows a clear divergence between the most productive areas in terms of FLUXCOM GPP, the equatorial rainforests of Brazil, central Africa and Indonesia, and the regions with the highest levels of downscaled SIF, the croplands of the mid-West, Western Europe and South America.

Equatorial broadleaf forests are also areas with reduced spatio-temporal correlation and scaling between SIF_{DS} and GPP_{FX}, as seen in figure 3, with some areas anti-correlated. Figure 5 shows that the high variance in downscaled SIF is not matched by the similarly wide variation in FLUXCOM GPP observed in other vegetation types resulting in a flat relationship. This may hint at a saturation at high values of GPP_{FX}, whereby the observed SIF_{DS} increases without a corresponding increase in GPP_{FX} at the same rate. Such a plateau, particularly in evergreen broadleaf forests, could be driven by the saturation of the fraction of absorbed photosynthetically active radiation at high LAI values or perhaps by constraints in the GPP_{FX} model. Indeed the largest uncertainty in the FLUXCOM dataset is found in the tropics, an area with limited FLUXNET sites, and a similarly low correlation has been observed between SIF_{DS} and GPP_{FX} on a seasonal scale (Jung et al., 2020). A similar, if slightly reduced, plateau in the spatial SIF_{DS}-GPP_{FX} relationship in evergreen needleleaf forests supports evidence of non-linearity in the temporal relationship found in Kim et al. (2021), similarly attributed to GPP_{FX} saturation (as measured via an eddy covariance system) with absorbed photosynthetically active radiation.

555   The comparatively higher values of SIF_{DS} in productive farm-belts supports evidence, such as in Guanter et al. (2014), that SIF-based crop productivity estimates are higher than other GPP estimates. The distribution of C3 and C4 crops may play a role here, as demonstrated by Zhang et al. (2017), which finds an underestimation of the FLUXCOM GPP in cropland areas, in addition to an overestimation in tropical rainforests. It may therefore be the case that the downscaled SIF is more sensitive to C3/C4 differences than the FLUXCOM GPP model. Additionally some studies, such as He et al. (2020) <u>and Li and Xiao (2022)</u>

560   , show more linearity between SIF and GPP in C4 crops, compared to C3 crops, with GPP estimated by eddy covariance towers. Differences in crop cover impacting the SIF_{DS}-GPP_{FX} scaling may also be seen in figure 7. For example, in East Asia, there is an under-estimate of productivity based on the global SIF_{DS}-GPP_{FX} relationship, and local measurements of downscaled SIF, whilst there is an over-estimate in the Americas, Africa and Europe.

    The divergences between SIF_{DS} and GPP_{FX} may partially be attributed to the procedures used to collect and model the input

565   data, however the divergences also support growing evidence of physiological reasons for the SIF_{DS}-GPP_{FX} differences. This suggests that downscaled SIF could provide added value to the FLUXCOM estimate of the GPP in certain regions where the characterization of vegetation based on FaPAR and functional types in the machine learning framework is not sufficient to capture the spatio-temporal pattern of primary productivity.

5.3   The universality of the SIF_{DS}-GPP_{FX} relationship across vegetation covers

570   Differences in the spatio-temporal SIF_{DS}-GPP_{FX} correlation and linear relationship suggests that there is some deviation, on average, between vegetation covers. However, there is also substantial variability within vegetation groupings, meaning that for all except the clearest outliers, it is not possible to statistically distinguish between vegetation categories based on these deviations alone. Equatorial evergreen broadleaf forests clearly stand out as an outlier~~having~~<u>, with</u> a spatio-temporal SIF_{DS}-GPP_{FX} relationship that is divergent from the other vegetation types and should be treated separately when projecting estimates

575   of productivity from SIF, until the reasons for this divergence are fully accounted for. For the other vegetation covers with SIF_{DS}-GPP_{FX} relationships that scale more linearly, there is no fixed η^2 threshold to categorically dictate when the vegetation categorisation plays an important role in distinguishing between the SIF_{DS}-GPP_{FX} relationships. This is particularly true in cases where the difference in the slope is small (η) but significant (p-value), whilst the difference in the intercept is large. ~~However, the results of the ANCOVA provide evidence that some distinction can be made between the SIF_{DS}-GPP_{FX} scaling~~

580   ~~between certain categories of vegetation, like temperate deciduous broadleaf forests, continental needleaf forests, and tropical evergreen forests.~~ Additionally, the intercept in the linear relationship tends to be slightly higher for woody trees compared to the herbaceous species and therefore a categorisation could loosely divide along this broad physiological plant trait.

    <u>The universality of the SIF-GPP relationship with respect to vegetation groupings is in area of active debate (Turner et al., 2021; Li and X</u> <u>.</u> Differences between vegetation covers likely result from differences is the canopy architecture and physiology, in particular

585   the leaf clustering, chlorophyll content and maximum carboxylation capacity (Verrelst et al., 2015). This is particularly true for differences between ~~herbaceaous~~ <u>herbaceous</u> and woody vegetation, where for the latter, the lower photon escape probability from the canopy results in a lower intensity of SIF for a given productivity. Additionally, as discussed previously, further disaggregation of vegetation covers may be beneficial, for example distinguishing between deciduous broadleaf forests in Northern

and Southern hemispheres, and between C3/C4 vegetation. Indeed it may be the case that there are more differences within certain vegetation covers, than between vegetation covers, and this effect may depend on the scale of the analysis. It is important to note however, that vegetation cover in the analysis may partially be a proxy for other factors or regional variables, such as background climate conditions and soil properties (Reichstein et al., 2014).

Distinctions between vegetation covers in the SIF_{DS} response to meteorological ~~stress~~ fluctuations shows the divide is broadly along these lines of woody vs non-woody vegetation types. Herbaceous plants are more susceptible to changes in water supply than woody species, universally preferring high soil moisture and low vapour pressure deficit in all environments. For woody trees, vapour pressure deficit tends to be more important than soil moisture, and plays very little role at all in the SIF_{DS} response of tropical evergreen broadleaf forests. This highlights the importance of using soil moisture, in addition to VPD, in quantifying droughts, and in particular its impacts on herbaceous vegetation (Stocker et al., 2018). Additionally, herbaceous species tend to respond stronger to meteorological fluctuations, with the exception of needleleaf forests. Overall, the study shows that it is possible to draw a distinction in the SIF_{DS}-GPP_{FX} and SIF_{DS}-meteorological relationships between vegetation covers. These loosely divide between woody and herbaceous vegetation, with particular cases where further investigation is needed to fully understand the relationship dynamics.

6   Conclusions

This exploratory analysis confronts two ~~of the most recent~~ observation-based products that inform on the spatio-temporal variability of primary productivity at global scale, highlighting areas of coherence and divergence. Firstly, it demonstrates the utility of the Duveiller et al. (2020) downscaling method in providing a high-resolution SIF dataset that can be used as proxy for gross primary production for specific vegetation covers. Secondly, in highlighting areas of divergence, the study provides a remotely-sensed, independent comparison of downscaled SIF with the FLUXCOM GPP model. The relatively fine resolution of the downscaled SIF enables a global exploration of the spatio-temporal relationship between SIF_{DS} and GPP_{FX} at a level that distinguishes between differing vegetation cover types, enabling a categorisation of vegetation covers based on the SIF_{DS}-GPP_{FX} response. For the most part, the gradient of the spatial SIF_{DS}-GPP_{FX} response is similar between differing vegetation types, with the ~~exceptions of temperate deciduous~~ exception of equatorial broadleaf forests, and, potentially, slight exceptions in continental needleleaf forests and ~~, particularly, equatorial~~ temperate deciduous broadleaf forests. However, the GPP_{FX} systematic potential for a given SIF_{DS} observation displays more variation between species, with some divergence between woody and non-woody plants. The study provides both evidence for the spatio-temporal correlation between downscaled SIF and FLUXCOM GPP, with different climate and vegetation covers exhibiting variability in the SIF_{DS}-GPP_{FX} relationship. The temporal component of the SIF_{DS}-GPP_{FX} relationship is generally stronger than the spatial component, in particular at an intra-annual scale. Regions of climate and vegetation cover exhibiting high spatial correlation between SIF_{DS} and GPP_{FX} also tend to exhibit higher temporal correlation, suggesting that the mechanisms driving spatial and temporal variability are similar. Vegetation in some climates, such as tropical rainforests, shows divergence from linearity in the SIF_{DS}-GPP_{FX} relationship.

Here the downscaled SIF data may provide additional, independent information to the FLUXCOM model, particularly at high GPP$_{FX}$ values where the model may be at risk of saturation of photosynthetically active radiation.

The study also demonstrates the possibility of using near real-time satellite SIF measurements to study the response of vegetation to meteorological anomalies over short (monthly) timescales. Proving this technique at a global scale ~~provides evidence for the use of~~ demonstrates that high-resolution SIF ~~in monitoring the resilience of local ecosystems to environmental fluctuations , an area of growing importance as extreme weather events become more frequent and more severe~~responds to meteorological fluctuations in a similar way to FLUXCOM GPP. As such it has potential as a near real-time indicator of vegetation status that, unlike FLUXCOM GPP, is independent of meteorological variables on aggregate. Whilst there is similarity in the SIF$_{DS}$-GPP$_{FX}$ response between vegetation covers, there is more diversity between different vegetation covers in the SIF$_{DS}$ response to meteorological fluctuations, particularly between herbaceous species and woody trees.

The further collection of high-resolution SIF data via the downscaling method of Duveiller et al. (2020) in addition to satellites such as OCO-2 and the future FLEX mission, will continue aid the understanding of the relationship between SIF, environmental conditions and plant productivity, as well as the variety of response between vegetation covers. The benefit will be to advance our understanding and estimation of the Earth's productivity, on both a local and global level.

References

Allan, R. and Pereira, L.: Crop evapotranspiration-Guidelines for computing crop water requirements-FAO Irrigation and drainage paper 56, vol. 56, 1998.

Anav, A., Friedlingstein, P., Beer, C., Ciais, P., Harper, A., Jones, C., Murray-Tortarolo, G., Papale, D., Parazoo, N., Peylin, P., Piao, S., Sitch, S., Viovy, N., Wiltshire, A., and Zhao, M.: Spatio-temporal patterns of terrestrial gross primary production: A review, Reviews of Geophysics, 53, https://doi.org/10.1002/2015RG000483, 2015.

Baldocchi, D., Falge, E., Gu, L., Olson, R., Hollinger, D., Running, S., Anthoni, P., Bernhofer, C., Davis, K., Evans, R., Fuentes, J., Goldstein, A., Katul, G., Law, B., Lee, X., Malhi, Y., Meyers, T., Munger, W., Oechel, W., U, K. T. P., Pilegaard, K., Schmid, H. P., Valentini, R., Verma, S., Vesala, T., Wilson, K., and Wofsy, S.: FLUXNET: A New Tool to Study the Temporal and Spatial Variability of Ecosystem-Scale Carbon Dioxide, Water Vapor, and Energy Flux Densities, Bulletin of the American Meteorological Society, 82, 2415 – 2434, https://doi.org/10.1175/1520-0477(2001)082<2415:FANTTS>2.3.CO;2, https://journals.ametsoc.org/view/journals/bams/82/11/1520-0477_2001_082_2415_fantts_2_3_co_2.xml, 2001.

Bowling, D. R., Garcia, M. R., Magney, T., Logan, B. A., Frankenberg, C., Grossman, K., Stutz, J., Raczka, B. M., Lopez, S., Burns, S. P., Blanken, P., and Lin, J. C.: Linkage between SIF and GPP in a seasonally-dormant high-elevation subalpine forest, in: AGU Fall Meeting Abstracts, vol. 2018, pp. B31N–2676, 2018.

CCI, E.: ESA: Land Cover CCI Product User Guide Version 2.0, http://maps.elie.ucl.ac.be/CCI/viewer/download/ESACCI-LC-Ph2-PUGv2_2.0.pdf, 2017.

Coppo, P., Taiti, A., Pettinato, L., Francois, M., Taccola, M., and Drusch, M.: Fluorescence Imaging Spectrometer (FLORIS) for ESA FLEX Mission, Remote Sensing, 9, 649, https://doi.org/10.3390/rs9070649, http://dx.doi.org/10.3390/rs9070649, 2017.

Defourny, P.: Land cover classification gridded maps from 1992 to present derived from satellite observations., https://doi.org/D3.3.11-v1.0_PUGS_CDR_LC-CCI_v2.0.7cds_Products_v1.0., https://cds.climate.copernicus.eu/cdsapp#!/dataset/satellite-land-cover?tab=overview, 2019.

Didan, K., A. B.: NASA MEaSUREs Vegetation Index and Phenology (VIP) Phenology NDVI Yearly Global $0.05°$ CMG., https://doi.org/https://doi.org/10.5067/MEaSUREs/VIP/VIPPHEN_NDVI.004. Accessed 2020-01-31, 2016.

Doughty, R., Köhler, P., Frankenberg, C., Magney, T. S., Xiao, X., Qin, Y., Wu, X., and Moore, B.: TROPOMI reveals dry-season increase of solar-induced chlorophyll fluorescence in the Amazon forest, Proceedings of the National Academy of Sciences, 116, 22 393–22 398, https://doi.org/10.1073/pnas.1908157116, https://www.pnas.org/doi/abs/10.1073/pnas.1908157116, 2019.

Duveiller, G. and Cescatti, A.: Spatially downscaling sun-induced chlorophyll fluorescence leads to an improved temporal correlation with gross primary productivity, Remote Sensing of Environment, 182, 72 – 89, https://doi.org/https://doi.org/10.1016/j.rse.2016.04.027, http://www.sciencedirect.com/science/article/pii/S0034425716301936, 2016.

Duveiller, G., Filipponi, F., Walther, S., Köhler, P., Frankenberg, C., Guanter, L., and Cescatti, A.: A spatially downscaled sun-induced fluorescence global product for enhanced monitoring of vegetation productivity, Earth System Science Data, 12, 1101–1116, https://doi.org/10.5194/essd-12-1101-2020, https://essd.copernicus.org/articles/12/1101/2020/, 2020.

Frankenberg, C. and Berry, J.: Solar Induced Chlorophyll Fluorescence: Origins, Relation to Photosynthesis and Retrieval, p. 143, https://doi.org/10.1016/B978-0-12-409548-9.10632-3, 2017.

670 Frankenberg, C., Butz, A., and Toon, G. C.: Disentangling chlorophyll fluorescence from atmospheric scattering effects in O2 A-band spectra of reflected sun-light, Geophysical Research Letters, 38, https://doi.org/https://doi.org/10.1029/2010GL045896, https://agupubs.onlinelibrary.wiley.com/doi/abs/10.1029/2010GL045896, 2011a.

Frankenberg, C., Fisher, J. B., Worden, J., Badgley, G., Saatchi, S. S., Lee, J.-E., Toon, G. C., Butz, A., Jung, M., Kuze, A., and Yokota, T.: New global observations of the terrestrial carbon cycle from GOSAT: Patterns of plant fluorescence with gross primary productivity, Geo-

675 physical Research Letters, 38, https://doi.org/https://doi.org/10.1029/2011GL048738, https://agupubs.onlinelibrary.wiley.com/doi/abs/10.1029/2011GL048738, 2011b.

Friedlingstein, P., Jones, M. W., O'Sullivan, M., Andrew, R. M., Hauck, J., Peters, G. P., Peters, W., Pongratz, J., Sitch, S., Le Quéré, C., Bakker, D. C. E., Canadell, J. G., Ciais, P., Jackson, R. B., Anthoni, P., Barbero, L., Bastos, A., Bastrikov, V., Becker, M., Bopp, L., Buitenhuis, E., Chandra, N., Chevallier, F., Chini, L. P., Currie, K. I., Feely, R. A., Gehlen, M., Gilfillan, D., Gkritzalis, T., Goll, D. S.,

680 Gruber, N., Gutekunst, S., Harris, I., Haverd, V., Houghton, R. A., Hurtt, G., Ilyina, T., Jain, A. K., Joetzjer, E., Kaplan, J. O., Kato, E., Klein Goldewijk, K., Korsbakken, J. I., Landschützer, P., Lauvset, S. K., Lefèvre, N., Lenton, A., Lienert, S., Lombardozzi, D., Marland, G., McGuire, P. C., Melton, J. R., Metzl, N., Munro, D. R., Nabel, J. E. M. S., Nakaoka, S.-I., Neill, C., Omar, A. M., Ono, T., Peregon, A., Pierrot, D., Poulter, B., Rehder, G., Resplandy, L., Robertson, E., Rödenbeck, C., Séférian, R., Schwinger, J., Smith, N., Tans, P. P., Tian, H., Tilbrook, B., Tubiello, F. N., van der Werf, G. R., Wiltshire, A. J., and Zaehle, S.: Global Carbon Budget 2019, Earth System

685 Science Data, 11, 1783–1838, https://doi.org/10.5194/essd-11-1783-2019, https://www.earth-syst-sci-data.net/11/1783/2019/, 2019.

Gensheimer, J., Turner, A. J., Köhler, P., Frankenberg, C., and Chen, J.: A convolutional neural network for spatial downscaling of satellite-based solar-induced chlorophyll fluorescence (SIFnet), Biogeosciences, 19, 1777–1793, https://doi.org/10.5194/bg-19-1777-2022, https://bg.copernicus.org/articles/19/1777/2022/, 2022.

Gentine, P. and Alemohammad, H.: RSIF (Reconstructed Solar Induced Fluorescence): a machine-learning vegetation product

690 based on MODIS surface reflectance to reproduce GOME-2 solar induced fluorescence, Geophysical Research Letters, 45, https://doi.org/10.1002/2017GL076294, 2018.

Grossiord, C., Buckley, T. N., Cernusak, L. A., Novick, K. A., Poulter, B., Siegwolf, R. T. W., Sperry, J. S., and McDowell, N. G.: Plant responses to rising vapor pressure deficit, New Phytologist, 226, 1550–1566, https://doi.org/https://doi.org/10.1111/nph.16485, https://nph.onlinelibrary.wiley.com/doi/abs/10.1111/nph.16485, 2020.

695 Guanter, L., Frankenberg, C., Dudhia, A., Lewis, P. E., Gómez-Dans, J., Kuze, A., Suto, H., and Grainger, R. G.: Retrieval and global assessment of terrestrial chlorophyll fluorescence from GOSAT space measurements, Remote Sensing of Environment, 121, 236–251, https://doi.org/https://doi.org/10.1016/j.rse.2012.02.006, https://www.sciencedirect.com/science/article/pii/S0034425712000909, 2012.

Guanter, L., Zhang, Y., Jung, M., Joanna, J., Voigt, M., Berry, J., Frankenberg, C., Huete, A., Zarco-Tejada, P., Lee, J.-E., Moran, M., Ponce-Campos, G., Beer, C., Camps-Valls, G., Buchmann, N., Gianelle, D., Klumpp, K., Cescatti, A., Baker, J., and Griffis, T.: Global and

700 time-resolved monitoring of crop photosynthesis with chlorophyll fluorescence, Proceedings of the National Academy of Sciences, p. 1, https://doi.org/10.1073/pnas.1320008111, 2014.

Guanter, L., Bacour, C., Schneider, A., Aben, I., van Kempen, T. A., Maignan, F., Retscher, C., Köhler, P., Frankenberg, C., Joiner, J., and Zhang, Y.: The TROPOSIF global sun-induced fluorescence dataset from the Sentinel-5P TROPOMI mission, Earth System Science Data, 13, 5423–5440, https://doi.org/10.5194/essd-13-5423-2021, https://essd.copernicus.org/articles/13/5423/2021/, 2021.

705 He, L., Magney, T., Dutta, D., Yin, Y., Köhler, P., Grossmann, K., Stutz, J., Dold, C., Hatfield, J., Guan, K., Peng, B., and Frankenberg, C.: From the Ground to Space: Using Solar-Induced Chlorophyll Fluorescence to Estimate Crop Productivity, Geophysical Research

Letters, 47, e2020GL087 474, https://doi.org/https://doi.org/10.1029/2020GL087474, https://agupubs.onlinelibrary.wiley.com/doi/abs/10.1029/2020GL087474, e2020GL087474 2020GL087474, 2020.

Jiao, W., Chang, Q., and Wang, L.: The Sensitivity of Satellite Solar-Induced Chlorophyll Fluorescence to Meteorological Drought,
710   Earth's Future, 7, 558–573, https://doi.org/https://doi.org/10.1029/2018EF001087, https://agupubs.onlinelibrary.wiley.com/doi/abs/10.1029/2018EF001087, 2019.

Joiner, J. and Yoshida, Y.: Global MODIS and FLUXNET-derived Daily Gross Primary Production, V2, https://doi.org/10.3334/ORNLDAAC/1835, https://daac.ornl.gov/cgi-bin/dsviewer.pl?ds_id=1835, 2021.

Joiner, J., Yoshida, Y., Vasilkov, A. P., Yoshida, Y., Corp, L. A., and Middleton, E. M.: First observations of global and seasonal terres-
715   trial chlorophyll fluorescence from space, Biogeosciences, 8, 637–651, https://doi.org/10.5194/bg-8-637-2011, https://bg.copernicus.org/articles/8/637/2011/, 2011.

Joiner, J., Yoshida, Y., Vasilkov, A. P., Middleton, E. M., Campbell, P. K. E., Yoshida, Y., Kuze, A., and Corp, L. A.: Filling-in of near-infrared solar lines by terrestrial fluorescence and other geophysical effects: simulations and space-based observations from SCIAMACHY and GOSAT, Atmospheric Measurement Techniques, 5, 809–829, https://doi.org/10.5194/amt-5-809-2012, https://amt.copernicus.org/articles/
720   5/809/2012/, 2012.

Joiner, J., Guanter, L., Lindstrot, R., Voigt, M., Vasilkov, A. P., Middleton, E. M., Huemmrich, K. F., Yoshida, Y., and Frankenberg, C.: Global monitoring of terrestrial chlorophyll fluorescence from moderate-spectral-resolution near-infrared satellite measurements: methodology, simulations, and application to GOME-2, Atmospheric Measurement Techniques, 6, 2803–2823, https://doi.org/10.5194/amt-6-2803-2013, https://www.atmos-meas-tech.net/6/2803/2013/, 2013.

725 Jung, M. and FLUXCOM Team: FLUXCOM (RS+METEO) Global Land Carbon Fluxes using CRUNCEP climate data, https://doi.org/10.17871/FLUXCOM_RS_METEO_CRUNCEPV6_1980_2013_V1, https://www.bgc-jena.mpg.de/geodb/FluxCom/RS_METEO_CRUNCEPv6_1980_2013_v1.php, 2016.

Jung, M., Koirala, S., Weber, U., Ichii, K., Gans, F., Gustau-Camps-Valls, Papale, D., Schwalm, C., Tramontana, G., and Reichstein, M.: The FLUXCOM ensemble of global land-atmosphere energy fluxes, Sci Data, 6, https://doi.org/10.1038/s41597-019-0076-8, https://doi.org/
730   10.1038/s41597-019-0076-8, 2019.

Jung, M., Schwalm, C., Migliavacca, M., Walther, S., Camps-Valls, G., Koirala, S., Anthoni, P., Besnard, S., Bodesheim, P., Carvalhais, N., Chevallier, F., Gans, F., Goll, D. S., Haverd, V., Köhler, P., Ichii, K., Jain, A. K., Liu, J., Lombardozzi, D., Nabel, J. E. M. S., Nelson, J. A., O'Sullivan, M., Pallandt, M., Papale, D., Peters, W., Pongratz, J., Rödenbeck, C., Sitch, S., Tramontana, G., Walker, A., Weber, U., and Reichstein, M.: Scaling carbon fluxes from eddy covariance sites to globe: synthesis and evaluation of the FLUXCOM approach,
735   Biogeosciences, 17, 1343–1365, https://doi.org/10.5194/bg-17-1343-2020, https://www.biogeosciences.net/17/1343/2020/, 2020.

Kim, J., Ryu, Y., Dechant, B., Lee, H., Kim, H. S., Kornfeld, A., and Berry, J. A.: Solar-induced chlorophyll fluorescence is non-linearly related to canopy photosynthesis in a temperate evergreen needleleaf forest during the fall transition, Remote Sensing of Environment, 258, 112 362, https://doi.org/https://doi.org/10.1016/j.rse.2021.112362, https://www.sciencedirect.com/science/article/pii/S0034425721000808, 2021.

740 Köhler, P., Guanter, L., and Joiner, J.: A linear method for the retrieval of sun-induced chlorophyll fluorescence from GOME-2 and SCIAMACHY data, Atmospheric Measurement Techniques, 8, 2589–2608, https://doi.org/10.5194/amt-8-2589-2015, https://www.atmos-meas-tech.net/8/2589/2015/, 2015.

Kottek, M., Grieser, J., Beck, C., Rudolf, B., and Rubel, F.: World Map of the Köppen-Geiger climate classification updated, Meteorologische Zeitschrift, 15, 259–263, https://doi.org/10.1127/0941-2948/2006/0130, http://dx.doi.org/10.1127/0941-2948/2006/0130, 2006.

745 Köhler, P., Frankenberg, C., Magney, T. S., Guanter, L., Joiner, J., and Landgraf, J.: Global Retrievals of Solar-Induced Chlorophyll Fluorescence With TROPOMI: First Results and Intersensor Comparison to OCO-2, Geophysical Research Letters, 45, 10,456–10,463, https://doi.org/https://doi.org/10.1029/2018GL079031, https://agupubs.onlinelibrary.wiley.com/doi/abs/10.1029/2018GL079031, 2018a.

Köhler, P., Frankenberg, C., Magney, T. S., Guanter, L., Joiner, J., and Landgraf, J.: Global Retrievals of Solar-Induced Chlorophyll Fluorescence With TROPOMI: First Results and Intersensor Comparison to OCO-2, Geophysical Research Letters, 45, 10,456–10,463,
750 https://doi.org/https://doi.org/10.1029/2018GL079031, https://agupubs.onlinelibrary.wiley.com/doi/abs/10.1029/2018GL079031, 2018b.

Lee, J.-E., Frankenberg, C., van der Tol, C., Berry, J. A., Guanter, L., Boyce, C. K., Fisher, J. B., Morrow, E., Worden, J. R., Asefi, S., Badgley, G., and Saatchi, S.: Forest productivity and water stress in Amazonia: observations from GOSAT chlorophyll fluorescence, Proceedings of the Royal Society B: Biological Sciences, 280, 20130 171, https://doi.org/10.1098/rspb.2013.0171, https://royalsocietypublishing.org/doi/abs/10.1098/rspb.2013.0171, 2013.

755 Li, X. and Xiao, J.: A Global, 0.05-Degree Product of Solar-Induced Chlorophyll Fluorescence Derived from OCO-2, MODIS, and Reanalysis Data, Remote Sensing, 11, 517, https://doi.org/10.3390/rs11050517, 2019.

Li, X. and Xiao, J.: TROPOMI observations allow for robust exploration of the relationship between solar-induced chlorophyll fluorescence and terrestrial gross primary production, Remote Sensing of Environment, 268, 112 748, https://doi.org/https://doi.org/10.1016/j.rse.2021.112748, https://www.sciencedirect.com/science/article/pii/S0034425721004685, 2022.

760 Magney, T., Bowling, D., Logan, B., Grossmann, K., Stutz, J., Blanken, P., Burns, S., Cheng, R., Garcia, M., Köhler, P., Lopez, S., Parazoo, N., Raczka, B., Schimel, D., and Frankenberg, C.: Mechanistic evidence for tracking the seasonality of photosynthesis with solar-induced fluorescence, Proceedings of the National Academy of Sciences of the United States of America, 116, https://doi.org/10.1073/pnas.1900278116, 2019.

Magney, T. S., Barnes, M. L., and Yang, X.: On the Covariation of Chlorophyll Fluorescence and Photosynthesis Across Scales, Geophysical
765 Research Letters, 47, e2020GL091 098, https://doi.org/https://doi.org/10.1029/2020GL091098, https://agupubs.onlinelibrary.wiley.com/doi/abs/10.1029/2020GL091098, e2020GL091098 2020GL091098, 2020.

Muñoz Sabater, J., Dutra, E., Agustí-Panareda, A., Albergel, C., Arduini, G., Balsamo, G., Boussetta, S., Choulga, M., Harrigan, S., Hersbach, H., Martens, B., Miralles, D. G., Piles, M., Rodríguez-Fernández, N. J., Zsoter, E., Buontempo, C., and Thépaut, J.-N.: ERA5-Land: A state-of-the-art global reanalysis dataset for land applications, Earth System Science Data Discussions, 2021, 1–50,
770 https://doi.org/10.5194/essd-2021-82, https://essd.copernicus.org/preprints/essd-2021-82/, 2021.

Muñoz Sabater, J.: ERA5-Land hourly data from 1981 to present., https://doi.org/10.24381/cds.e2161bac, https://cds.climate.copernicus.eu/cdsapp#!/dataset/reanalysis-era5-land?tab=overview, 2019a.

Muñoz Sabater, J.: ERA5-Land monthly averaged data from 1981 to present., https://doi.org/10.24381/cds.68d2bb3, https://cds.climate.copernicus.eu/cdsapp#!/dataset/reanalysis-era5-land-monthly-means?tab=overview, 2019b.

775 Pei, Y., Dong, J., Zhang, Y., Yuan, W., Doughty, R., Yang, J., Zhou, D., Zhang, L., and Xiao, X.: Evolution of light use efficiency models: Improvement, uncertainties, and implications, Agricultural and Forest Meteorology, 317, 108 905, https://doi.org/10.1016/j.agrformet.2022.108905, 2022.

Ploton, P., Mortier, F., Réjou-Méchain, M., Barbier, N., Picard, N., Rossi, V., Dormann, C., Cornu, G., Viennois, G., Bayol, N., Lyapustin, A., Gourlet-Fleury, S., and Pélissier, R.: Spatial validation reveals poor predictive performance of large-scale ecological mapping models,
780 Nature Communications, 11, 4540, https://doi.org/10.1038/s41467-020-18321-y, https://doi.org/10.1038/s41467-020-18321-y, 2020.

Porcar-Castell, A., Tyystjärvi, E., Atherton, J., van der Tol, C., Flexas, J., Pfündel, E. E., Moreno, J., Frankenberg, C., and Berry, J. A.: Linking chlorophyll a fluorescence to photosynthesis for remote sensing applications: mechanisms and challenges, Journal of Experimental Botany, 65, 4065–4095, https://doi.org/10.1093/jxb/eru191, https://doi.org/10.1093/jxb/eru191, 2014.

Reichstein, M., Bahn, M., Mahecha, M. D., Kattge, J., and Baldocchi, D. D.: Linking plant and ecosystem functional biogeography, Proceedings of the National Academy of Sciences, 111, 13 697–13 702, https://doi.org/10.1073/pnas.1216065111, https://www.pnas.org/doi/abs/10.1073/pnas.1216065111, 2014.

Rubel, F. and Kottek, M.: Observed and projected climate shifts 1901-2100 depicted by world maps of the Köppen-Geiger climate classification, Meteorologische Zeitschrift, 19, 135–141, https://doi.org/10.1127/0941-2948/2010/0430, http://dx.doi.org/10.1127/0941-2948/2010/0430, 2010.

Rubel, F., Brugger, K., Haslinger, K., and Auer, I.: The climate of the European Alps: Shift of very high resolution Köppen-Geiger climate zones 1800–2100, Meteorologische Zeitschrift, 26, 115–125, https://doi.org/10.1127/metz/2016/0816, 2017.

Running, S. W., Nemani, R. R., Heinsch, F. A., Zhao, M., Reeves, M., and Hashimoto, H.: A Continuous Satellite-Derived Measure of Global Terrestrial Primary Production, BioScience, 54, 547–560, https://doi.org/10.1641/0006-3568(2004)054[0547:ACSMOG]2.0.CO;2, https://doi.org/10.1641/0006-3568(2004)054[0547:ACSMOG]2.0.CO;2, 2004.

Ryu, Y., Berry, J., and Baldocchi, D.: What is global photosynthesis? History, uncertainties and opportunities, Remote Sensing of Environment, 223, 95–114, https://doi.org/10.1016/j.rse.2019.01.016, 2019.

Seneviratne, S.I., Nicholls, N., Easterling, D., Goodess, C., Kanae, S., Kossin, J., Luo, Y., Marengo, J., McInnes, K., andM. Reichstein, M. R., Sorteberg, A., Vera, C., , and Zhang, X.: Managing the Risks of Extreme Events and Disasters to Advance Climate Change Adaptation, A Special Report of Working Groups I and II of the Intergovernmental Panel on ClimateChange (IPCC). Cambridge University Press, Cambridge, UK, and New York, NY, USA,, Changes in climate extremes and their impacts on the naturalphysical environment, 109–230, https://www.ipcc.ch/site/assets/uploads/2018/03/SREX-Chap3_FINAL-1.pdf, 2012.

Stocker, B. D., Zscheischler, J., Keenan, T. F., Prentice, I. C., Peñuelas, J., and Seneviratne, S. I.: Quantifying soil moisture impacts on light use efficiency across biomes, New Phytologist, 218, 1430–1449, https://doi.org/https://doi.org/10.1111/nph.15123, https://nph.onlinelibrary.wiley.com/doi/abs/10.1111/nph.15123, 2018.

Sun, Y., Frankenberg, C., Jung, M., Joanna, J., Guanter, L., Köhler, P., and Magney, T.: Overview of Solar-Induced chlorophyll Fluorescence (SIF) from the Orbiting Carbon Observatory-2: Retrieval, cross-mission comparison, and global monitoring for GPP, Remote Sensing of Environment, 209, https://doi.org/10.1016/j.rse.2018.02.016, 2018.

Tramontana, G., Jung, M., Schwalm, C. R., Ichii, K., Camps-Valls, G., Ráduly, B., Reichstein, M., Arain, M. A., Cescatti, A., Kiely, G., Merbold, L., Serrano-Ortiz, P., Sickert, S., Wolf, S., and Papale, D.: Predicting carbon dioxide and energy fluxes across global FLUXNET sites with regression algorithms, Biogeosciences, 13, 4291–4313, https://doi.org/10.5194/bg-13-4291-2016, https://www.biogeosciences.net/13/4291/2016/, 2016.

Turner, A. J., Köhler, P., Magney, T. S., Frankenberg, C., Fung, I., and Cohen, R. C.: Extreme events driving year-to-year differences in gross primary productivity across the US, Biogeosciences, 18, 6579–6588, https://doi.org/10.5194/bg-18-6579-2021, https://bg.copernicus.org/articles/18/6579/2021/, 2021.

Verrelst, J., Rivera, J. P., van der Tol, C., Magnani, F., Mohammed, G., and Moreno, J.: Global sensitivity analysis of the SCOPE model: What drives simulated canopy-leaving sun-induced fluorescence?, Remote Sensing of Environment, 166, 8–21, https://doi.org/https://doi.org/10.1016/j.rse.2015.06.002, https://www.sciencedirect.com/science/article/pii/S0034425715300328, 2015.

Walther, S., Duveiller, G., Jung, M., Guanter, L., Cescatti, A., and Camps-Valls, G.: Satellite Observations of the Contrasting Response of Trees and Grasses to Variations in Water Availability, Geophysical Research Letters, 46, 1429–1440, https://doi.org/https://doi.org/10.1029/2018GL080535, https://agupubs.onlinelibrary.wiley.com/doi/abs/10.1029/2018GL080535, 2019.

Yu, L., Wen, J., Chang, C., Frankenberg, C., and Sun, Y.: High Resolution Global Contiguous Solar-Induced Chlorophyll Fluorescence (SIF) of Orbiting Carbon Observatory-2 (OCO-2), Geophysical Research Letters, https://doi.org/10.1029/2018GL081109, 2018.

Zhang, Y., Guanter, L., Berry, J., Tol, C., Yang, X., Tang, J., and Zhang, F.: Model-based analysis of the relationship between sun-induced chlorophyll fluorescence and gross primary production for remote sensing applications, Remote Sensing of Environment, 187, https://doi.org/10.1016/j.rse.2016.10.016, 2016.

Zhang, Y., Xiao, X., Wu, X., Zhou, S., Zhang, G., Qin, Y., and Dong, J. a.: A global moderate resolution dataset of gross primary production of vegetation for 2000–2016, Scientific Data, 4, 170 165, https://doi.org/10.1038/sdata.2017.165, https://doi.org/10.1038/sdata.2017.165, 2017.

Zhang, Y., Joanna, J., Alemohammad, H., Zhou, S., and Gentine, P.: A global spatially contiguous solar-induced fluorescence (CSIF) dataset using neural networks, Biogeosciences, 15, 5779–5800, https://doi.org/10.5194/bg-15-5779-2018, 2018a.

Zhang, Y., Joiner, J., Gentine, P., and Zhou, S.: Reduced solar-induced chlorophyll fluorescence from GOME-2 during Amazon drought caused by dataset artifacts, Global Change Biology, 24, 2229–2230, https://doi.org/10.1111/gcb.14134, https://onlinelibrary.wiley.com/doi/abs/10.1111/gcb.14134, 2018b.

Álvaro Moreno-Martínez, Camps-Valls, G., Kattge, J., Robinson, N., Reichstein, M., van Bodegom, P., Kramer, K., Cornelissen, J. H. C., Reich, P., Bahn, M., Ülo Niinemets, Peñuelas, J., Craine, J. M., Cerabolini, B. E., Minden, V., Laughlin, D. C., Sack, L., Allred, B., Baraloto, C., Byun, C., Soudzilovskaia, N. A., and Running, S. W.: A methodology to derive global maps of leaf traits using remote sensing and climate data, Remote Sensing of Environment, 218, 69–88, https://doi.org/https://doi.org/10.1016/j.rse.2018.09.006, https://www.sciencedirect.com/science/article/pii/S0034425718304176, 2018.

Appendix A: Appendix

A1 Full ANCOVA results for downscaled SIF and FLUXCOM GPP

Table A1 contains the full results of the analysis of covariance for the SIF_{DS}-GPP_{FX} relationship between pairs of land covers. In each climate category, vegetation cover pairs with the largest η^2 for the slope are listed first, where the slope is significant (p-value < 0.05). If differences in the regression slope are not significant (i.e. the slopes are considered to be parallel), then the difference in the size of the effect of the intercept is considered, such that the lowest ranked pairs within a climate zone are the most similar in their SIF_{DS}-GPP_{FX} response.

Climate	land cover		slope		intercept	
	LC_1	LC_2	p-value	η^2	p-value	η^2
Equatorial	EBF	DBF	1.34×10^{-95}	0.19	$< 1.00\times10^{-99}$	0.53
Equatorial	EBF	GRA	1.59×10^{-77}	0.17	$< 1.00\times10^{-99}$	0.49
Equatorial	EBF	CRO	1.85×10^{-55}	0.12	$< 1.00\times10^{-99}$	0.49
Equatorial	DBF	CRO	1.53×10^{-01}	< 0.01	3.91×10^{-45}	0.10
Equatorial	DBF	GRA	1.36×10^{-01}	< 0.01	1.37×10^{-39}	0.09
Equatorial	GRA	CRO	8.38×10^{-01}	< 0.01	5.09×10^{-01}	< 0.01
Arid	GRA	DBF	4.35×10^{-28}	0.07	$< 1.00\times10^{-99}$	0.36
Arid	CRO	DBF	3.01×10^{-10}	0.02	6.88×10^{-91}	0.23
Arid	DBF	ENF	4.64×10^{-06}	0.02	1.75×10^{-05}	0.02
Arid	GRA	CRO	1.41×10^{-04}	0.01	3.14×10^{-36}	0.08
Arid	GRA	ENF	1.00×10^{-03}	0.01	6.46×10^{-79}	0.21
Arid	ENF	CRO	6.36×10^{-01}	< 0.01	4.27×10^{-05}	< 0.01
Temperate	DBF	ENF	4.09×10^{-56}	0.12	3.08×10^{-08}	0.02
Temperate	DBF	GRA	5.80×10^{-39}	0.08	$< 1.00\times10^{-99}$	0.50
Temperate	DBF	CRO	2.36×10^{-23}	0.05	5.81×10^{-86}	0.18
Temperate	EBF	DBF	1.80×10^{-19}	0.04	$< 1.00\times10^{-99}$	0.20
Temperate	ENF	GRA	1.77×10^{-12}	0.02	1.00×10^{-99}	0.56
Temperate	ENF	CRO	6.22×10^{-08}	0.02	$< 1.00\times10^{-99}$	0.27
Temperate	EBF	ENF	2.33×10^{-07}	0.01	2.25×10^{-42}	0.09
Temperate	EBF	GRA	9.52×10^{-01}	< 0.01	1.00×10^{-99}	0.68
Temperate	EBF	CRO	9.14×10^{-01}	< 0.01	$< 1.00\times10^{-99}$	0.47
Temperate	GRA	CRO	8.28×10^{-01}	< 0.01	1.55×10^{-63}	0.13
Continental	DBF	DNF	5.72×10^{-54}	0.11	1.71×10^{-07}	0.01
Continental	DNF	GRA	3.77×10^{-49}	0.10	$< 1.00\times10^{-99}$	0.25
Continental	DBF	ENF	4.57×10^{-43}	0.09	9.59×10^{-11}	0.02
Continental	ENF	GRA	1.27×10^{-34}	0.07	$< 1.00\times10^{-99}$	0.60
Continental	DNF	CRO	1.54×10^{-26}	0.06	9.95×10^{-62}	0.13
Continental	DBF	CRO	9.06×10^{-23}	0.05	$< 1.00\times10^{-99}$	0.21
Continental	ENF	CRO	8.43×10^{-15}	0.03	$< 1.00\times10^{-99}$	0.42
Continental	DBF	GRA	1.66×10^{-11}	0.02	$< 1.00\times10^{-99}$	0.30
Continental	GRA	CRO	2.66×10^{-09}	0.02	4.24×10^{-14}	0.03
Continental	ENF	DNF	9.18×10^{-05}	0.01	$< 1.00\times10^{-99}$	0.32

Table A1. Analysis of covariance between pairs of land covers in different Köppen–Geiger climate groupings. ANCOVA is only performed on the intercept when the difference between slopes is not considered significant. In order to highlight areas of similarity and difference, the η^2 column, comparable to the percentage of the difference in the slope or intercept (the latter assuming equivalence of the slopes) attributable to the vegetation cover, is coloured green, yellow and red for the slope categories: ≤ 0.01, $0.02 - 0.05$, > 0.05; and the intercept categories: ≤ 0.01, $0.02 - 0.15$, > 0.15, respectively.

A2   FLUXCOM GPP response to meteorological fluctuations
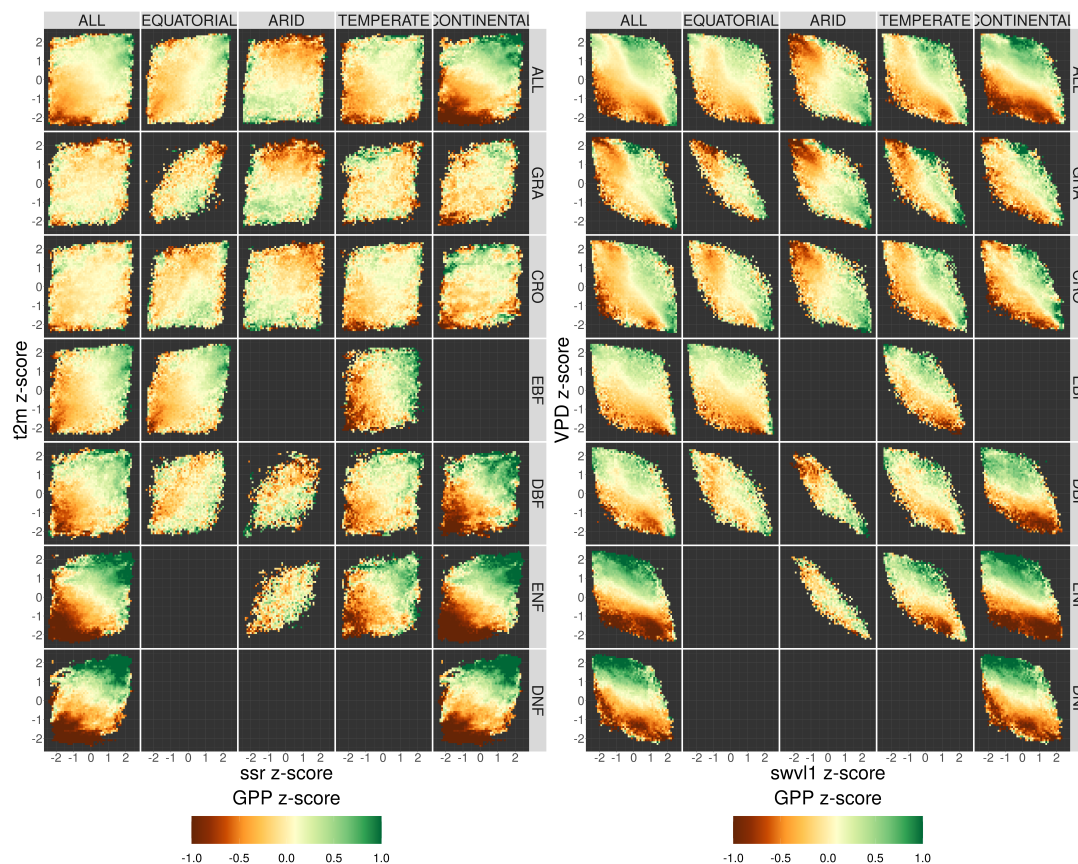

Figure A1. The relationship between fluctuations in meteorological variables and the corresponding fluctuations in the FLUXCOM GPP. The fluctuations are measured relative to the monthly mean for each pixel and expressed as a z-score. The four meteorological variables are air temperature and net surface solar radiation (t2m and ssr, left) and vapour pressure deficit and soil moisture (VPD and swvl1, right). The GPP$_{FX}$ response in each bin is the mean of all data points in each bin of meteorological z-score. The data is broken down into separate Köppen–Geiger climate zones and land cover categories.

A3   Comparison of downscaled SIF with FluxSat GPP

A3.1   FluxSat GPP data

The presented analysis is repeated with an alternative GPP product to verify that the conclusions drawn regarding the nature of the spatial SIF-GPP relationship are not unique to the dataset. FluxSat is a global $0.05°$ GPP estimate derived from the MODIS Nadir Bidirectional Reflectance Distribution Function (BRDF)-Adjusted Reflectances, input into neural networks that upscale GPP estimated from FLUXNET eddy covariance tower sites (Joiner and Yoshida, 2021).

The data is aggregated to 8-day time steps and the growing season GPP is averaged over the period 2007-2014 in order to ensure compatibility with the downscaled SIF data. The pixels considered in the analysis are the same as those used in the main paper, and the methodology used is the same.

A3.2   FluxSat GPP distribution

Figure A2 shows the spatial distribution of the mean growing season FluxSat GPP and the difference to the mean growing season FLUXCOM GPP. The figure is comparable to that of downscaled SIF distribution, figure 2. The figures shows that there is a significant difference between FluxSat and FLUXCOM GPP across most of the world.
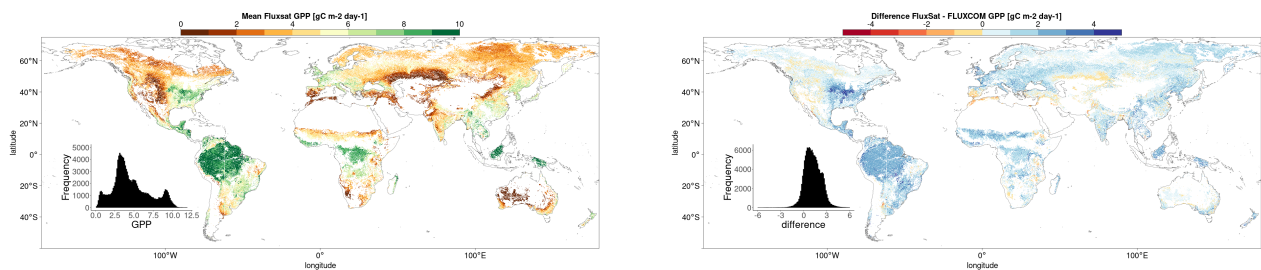

Figure A2. Left: The mean growing season FluxSat GPP 2007-2014. Right: The difference (FluxSat - FLUXCOM) between mean FluxSat GPP and mean FLUXCOM GPP (2007-2014).

A3.3   Spatial relationship between downscaled SIF and FluxSat GPP

Figure A3 shows the relative distribution and spatial linear relationship between the mean growing season FluxSat GPP as a function of the respective mean values of the downscaled SIF. The data are broken down into separate categories depending on the Köppen–Geiger climate grouping and dominant vegetation cover of the pixel. The figures show spatial correlations for the downscaled SIF and FluxSat GPP, are generally higher than those of the downscaled SIF and FLUXCOM GPP and so exhibit greater linearity.
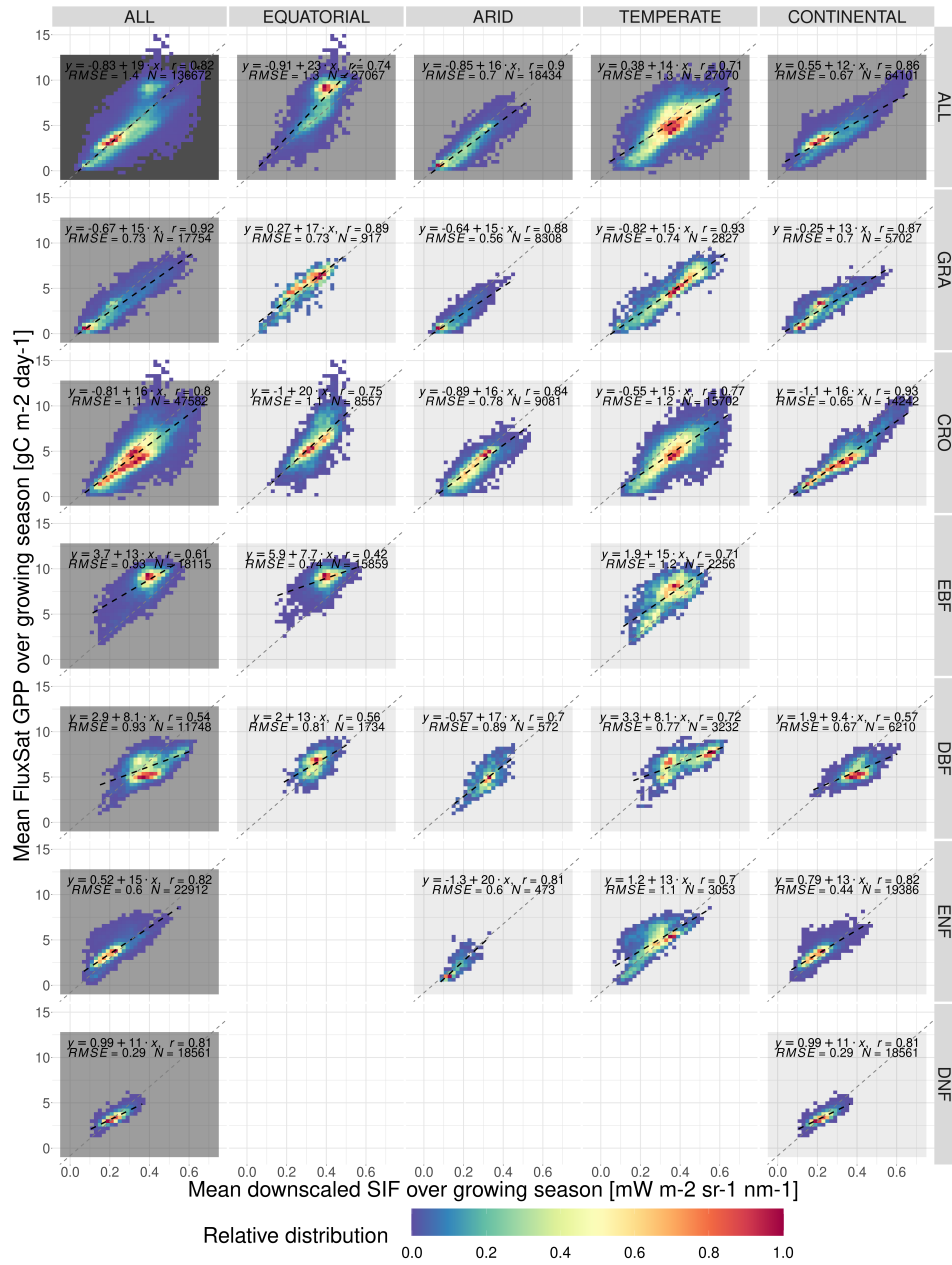
Figure A3. The spatial relationship between the mean growing season downscaled SIF and FluxSat GPP, broken down into separate Köppen–Geiger climate zones and vegetation cover categories. The plot shows the frequency distribution of pixels into SIF$_{DS}$-GPP$_{FX}$ bins, relative to the highest frequency bin in that category. A black dashed line representing a linear model in each category is overlaid and compared to a grey dotted line representing a linear model produced without the breakdown into separate categories (i.e. 'ALL-ALL'). The linear model equation, correlation coefficient r, root mean squared error (RMSE) and number of pixels are included.

A3.4 Spatial analysis of covariance between downscaled SIF and FluxSat GPP

The ANCOVA analysis is repeated for the downscaled SIF with FluxSat GPP, and the η^2 parameters for slope and intercept are displayed in figure A4, whilst the full results can be found in table A2.

The results support the analysis of covariance between the downscaled SIF and the FLUXCOM GPP. The difference in the SIF-GPP scaling between vegetation covers is relatively unimportant with a the exceptions of equatorial evergreen broadleaf forests and temperate deciduous broadleaf forests. Continental needleleaf forests are less of an exception when the FluxSat GPP is considered however. Indeed, in general, the differences between vegetation covers are less prominent with the FluxSat GPP. There is less difference in the scaling of the SIF-GPP relationship between land covers, than there is in the starting potential, with the significance and the magnitude of effect of the choice of vegetation covers on the intercept slightly greater in comparisons between a woody and a non-woody species, than within woody/non-woody groupings. This intercept is generally higher for woody vegetation.

A4   Comparison with TROPOMI SIF

A4.1   TROPOMI SIF data

As described in Duveiller et al. (2020) the downscaled SIF dataset is independently validated with OCO-2 SIF observations and, after bias correction, the resulting downscaled SIF data show high spatio-temporal agreement with the first SIF retrievals from the TROPOMI mission. Further comparison of the length-of-day corrected TROPOMI data with FLUXCOM GPP is provided to support the specific analysis presented in this paper (Guanter et al., 2021).

The TROPOMI data is averaged to 8-day time steps with the composite containing observations with a zenith angle below $40°$. The pixels considered in the analysis are the same as those used in the main paper, with the requirements on missing data points loosened to ensure coverage. Due to the shorter time span of available data from TROPOMI, only the 2020 dataset is analysed here. Additionally, the analysis differs from that presented in the paper as the coverage of the VIPPHEN phenology dataset does not extend to the years covered by TROPOMI and the growing season of 2014 - the final VIPPHEN year available - is used to define the growing season and compare SIF and GPP. Finally the comparison is made with an extended FLUXCOM GPP dataset which may contain methodological differences from that used in the paper.

A4.2   TROPOMI SIF distribution

Figure A5 shows the spatial distribution of the mean growing season TROPOMI SIF and the difference to the mean growing season downscaled SIF. The figure is comparable to that of downscaled SIF distribution, figure 2. TROPOMI generally shows a lower SIF than the downscaled values, with a mean difference of -0.077. These are relatively evenly distributed across the globe, with the exception of the tropics, which shows an excess in TROPOMI compared to downscaled SIF.
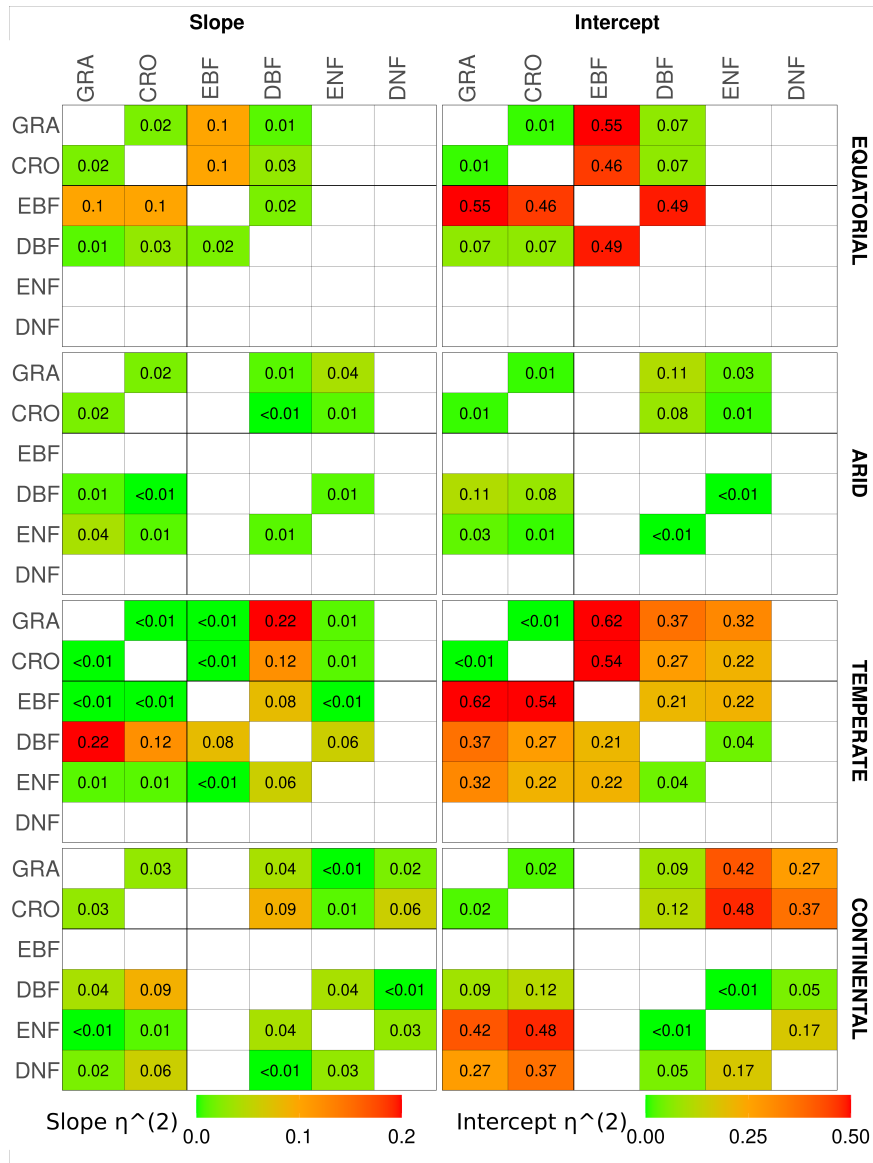
Figure A4. The η^2 parameter of an analysis of covariance between pairs of vegetation covers in different Köppen–Geiger climate groupings, for the slope (left) and intercept (right) of the linear relationship between downscaled SIF and FluxSat GPP. ANCOVA is performed on the intercept under the assumption that the difference between slopes is not significant. The η^2 parameter is comparable to the percentage of the difference in the slope or intercept (the latter assuming equivalence of the slopes) attributable to the difference in vegetation cover, with lower values signifying a smaller difference between vegetation covers. A slightly bolder line is used to separate the herbaceous species (CRO, GRA) from the woody species (EBF, DBF, ENF, DNF).

Climate	land cover LC$_1$	land cover LC$_2$	slope p-value	slope η^2	intercept p-value	intercept η^2
EQUATORIAL	EBF	DBF	6.24×10^{-11}	0.02	$< 1.00\times10^{-99}$	0.49
EQUATORIAL	EBF	GRA	1.82×10^{-46}	0.10	$< 1.00\times10^{-99}$	0.55
EQUATORIAL	EBF	CRO	2.82×10^{-48}	0.10	$< 1.00\times10^{-99}$	0.46
EQUATORIAL	DBF	CRO	3.50×10^{-15}	0.03	2.15×10^{-31}	0.07
EQUATORIAL	DBF	GRA	1.43×10^{-07}	0.01	1.23×10^{-31}	0.07
EQUATORIAL	GRA	CRO	4.85×10^{-09}	0.02	5.15×10^{-05}	0.01
ARID	GRA	DBF	6.80×10^{-06}	0.01	5.25×10^{-42}	0.11
ARID	CRO	DBF	4.02×10^{-01}	< 0.01	2.19×10^{-30}	0.08
ARID	DBF	ENF	1.40×10^{-02}	0.01	1.25×10^{-01}	< 0.01
ARID	GRA	CRO	2.14×10^{-08}	0.02	2.84×10^{-05}	0.01
ARID	GRA	ENF	3.98×10^{-16}	0.04	5.99×10^{-11}	0.03
ARID	ENF	CRO	8.20×10^{-05}	0.01	2.61×10^{-05}	0.01
TEMPERATE	DBF	ENF	4.00×10^{-27}	0.06	3.94×10^{-17}	0.04
TEMPERATE	DBF	GRA	$< 1.00\times10^{-99}$	0.22	$< 1.00\times10^{-99}$	0.37
TEMPERATE	DBF	CRO	4.62×10^{-57}	0.12	$< 1.00\times10^{-99}$	0.27
TEMPERATE	EBF	DBF	6.07×10^{-40}	0.08	$< 1.00\times10^{-99}$	0.21
TEMPERATE	ENF	GRA	1.59×10^{-06}	0.01	$< 1.00\times10^{-99}$	0.32
TEMPERATE	ENF	CRO	3.47×10^{-04}	0.01	$< 1.00\times10^{-99}$	0.22
TEMPERATE	EBF	ENF	9.00×10^{-03}	< 0.01	$< 1.00\times10^{-99}$	0.22
TEMPERATE	EBF	GRA	3.42×10^{-01}	< 0.01	$< 1.00\times10^{-99}$	0.62
TEMPERATE	EBF	CRO	5.23×10^{-01}	< 0.01	$< 1.00\times10^{-99}$	0.54
TEMPERATE	GRA	CRO	8.66×10^{-01}	< 0.01	9.95×10^{-01}	< 0.01
CONTINENTAL	DBF	DNF	3.00×10^{-03}	< 0.01	1.21×10^{-24}	0.05
CONTINENTAL	DNF	GRA	1.92×10^{-08}	0.02	$< 1.00\times10^{-99}$	0.27
CONTINENTAL	DBF	ENF	2.96×10^{-20}	0.04	6.30×10^{-02}	< 0.01
CONTINENTAL	ENF	GRA	1.79×10^{-01}	< 0.01	$< 1.00\times10^{-99}$	0.42
CONTINENTAL	DNF	CRO	4.35×10^{-29}	0.06	$< 1.00\times10^{-99}$	0.37
CONTINENTAL	DBF	CRO	4.96×10^{-43}	0.09	1.81×10^{-55}	0.12
CONTINENTAL	ENF	CRO	8.07×10^{-06}	0.01	$< 1.00\times10^{-99}$	0.48
CONTINENTAL	DBF	GRA	2.11×10^{-17}	0.04	2.72×10^{-44}	0.09
CONTINENTAL	GRA	CRO	1.07×10^{-13}	0.03	2.22×10^{-12}	0.02
CONTINENTAL	ENF	DNF	5.12×10^{-16}	0.03	3.44×10^{-81}	0.17

Table A2. Analysis of covariance between pairs of land covers in different Köppen–Geiger climate groupings for the relationship between downscaled SIF and FluxSat GPP. ANCOVA is only performed on the intercept when the difference between slopes is not considered significant. In order to highlight areas of similarity and difference, the η^2 column, comparable to the percentage of the difference in the slope or intercept (the latter assuming equivalence of the slopes) attributable to the vegetation cover, is coloured green, yellow and red for the slope categories: ≤ 0.01, $0.02 - 0.05$, > 0.05; and the intercept categories: ≤ 0.01, $0.02 - 0.15$, > 0.15, respectively.
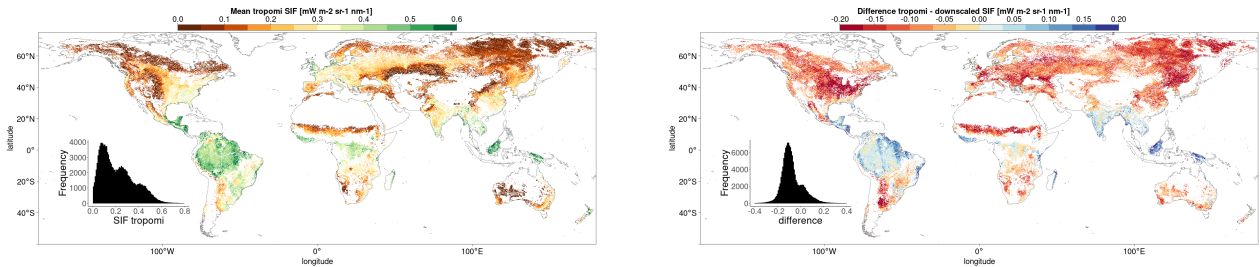

Figure A5. Left: The mean TROPOMI SIF in the 2020 growing season. Right: The difference (TROPOMI - downscaled) between mean TROPOMI SIF (2020) and mean downscaled SIF (2007-2014).

A4.3   Intra-annual correlation between TROPOMI SIF and FLUXCOM GPP

Figure A6 displays the intra-annual correlation between TROPOMI SIF and FLUXCOM GPP, as well as the difference (TROPOMI - downscaled) when compared to the intra-annual correlation between downscaled SIF and FLUXCOM GPP. The figure shows that across the growing season, the intra-annual correlation between TROPOMI SIF and FLUXCOM GPP is very similar to that of the downscaled SIF and GPP across a growing season, with the vast majority of points showing a difference of less that 0.1. Significant differences between the two SIF products are mostly observed in equatorial rainforests.
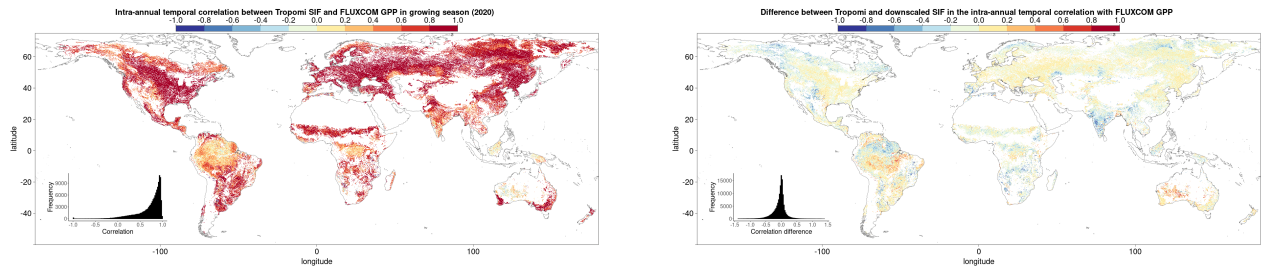

Figure A6. Left: The intra-annual temporal correlation between TROPOMI SIF and FLUXCOM GPP in 2020. Right: The difference (TROPOMI - downscaled) between TROPOMI SIF (2020) and downscaled SIF (2007-2014) in the intra-annual temporal correlation between SIF and FLUXCOM GPP.

A4.4   Spatial relationship between TROPOMI SIF and FLUXCOM GPP

Figure A7 shows the relative distribution and spatial linear relationship between the mean growing season FLUXCOM GPP as a function of the respective mean values of the TROPOMI SIF. The data are broken down into separate categories depending on the Köppen–Geiger climate grouping and dominant vegetation cover of the pixel. The figures show spatial correlations for the TROPOMI SIF and FLUXCOM GPP, that are broadly similar with those of the downscaled SIF and FLUXCOM GPP.

A4.5   Spatial analysis of covariance between TROPOMI SIF and FLUXCOM GPP

The ANCOVA analysis is repeated for the TROPOMI SIF with FLUXCOM GPP for the full year of 2020, and the η^2 parameters for slope and intercept are displayed in figure A8, whilst the full results can be found in table A3.

The results support the main features of the analysis with downscaled SIF seen in figure 6. The difference in the scaling of the SIF-GPP relationship (i.e. the slope) between vegetation covers is relatively unimportant. There are however, a few exceptions, the most significant of which is evergreen broadleaf forests in equatorial regions. The difference between deciduous broadleaf forests and other vegetation covers in temperate regions is no longer present, suggesting it may be a feature of the downscaled SIF. There is a slight distinction that can be drawn between the scaling of continental needleleaf forests and other vegetation covers. In general, there is a slight decrease in the differences between the vegetation covers in the TROPOMI SIF dataset.
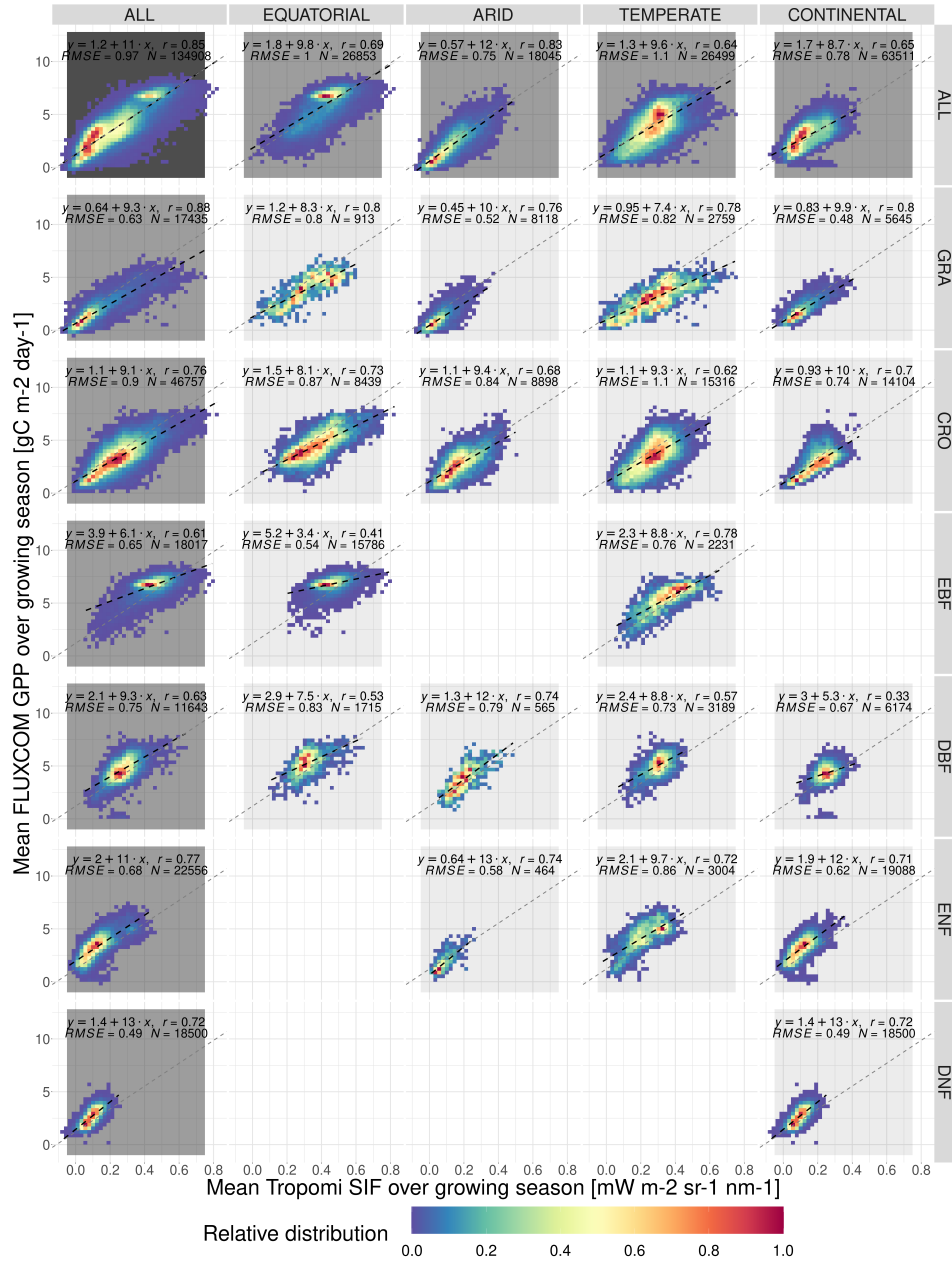
Figure A7. The spatial relationship between the mean growing season TROPOMI SIF and FLUXCOM GPP, broken down into separate Köppen–Geiger climate zones and vegetation cover categories. The plot shows the frequency distribution of pixels into SIF_{DS}-GPP_{FX} bins, relative to the highest frequency bin in that category. A black dashed line representing a linear model in each category is overlaid and compared to a grey dotted line representing a linear model produced without the breakdown into separate categories (i.e. 'ALL-ALL'). The linear model equation, correlation coefficient r, root mean squared error (RMSE) and number of pixels are included.

Climate	land cover LC$_1$	land cover LC$_2$	slope p-value	slope η^2	intercept p-value	intercept η^2
EQUATORIAL	EBF	DBF	1.13×10^{-22}	0.05	5.77×10^{-65}	0.14
EQUATORIAL	GRA	EBF	2.68×10^{-43}	0.10	$< 1.00\times10^{-99}$	0.59
EQUATORIAL	CRO	EBF	1.26×10^{-30}	0.06	$< 1.00\times10^{-99}$	0.54
EQUATORIAL	CRO	DBF	7.52×10^{-01}	< 0.01	$< 1.00\times10^{-99}$	0.30
EQUATORIAL	GRA	DBF	1.09×10^{-01}	< 0.01	$< 1.00\times10^{-99}$	0.42
EQUATORIAL	GRA	CRO	9.00×10^{-02}	< 0.01	1.16×10^{-08}	0.02
ARID	GRA	DBF	5.00×10^{-03}	< 0.01	7.84×10^{-88}	0.22
ARID	CRO	DBF	1.58×10^{-05}	0.01	1.98×10^{-68}	0.18
ARID	DBF	ENF	8.00×10^{-02}	< 0.01	4.98×10^{-16}	0.06
ARID	GRA	CRO	1.90×10^{-02}	< 0.01	1.60×10^{-27}	0.06
ARID	GRA	ENF	2.85×10^{-06}	0.01	2.53×10^{-39}	0.11
ARID	CRO	ENF	1.34×10^{-06}	0.02	4.50×10^{-01}	< 0.01
TEMPERATE	DBF	ENF	1.00×10^{-03}	< 0.01	9.40×10^{-01}	< 0.01
TEMPERATE	GRA	DBF	4.20×10^{-02}	< 0.01	$< 1.00\times10^{-99}$	0.58
TEMPERATE	CRO	DBF	7.10×10^{-02}	< 0.01	$< 1.00\times10^{-99}$	0.28
TEMPERATE	EBF	DBF	1.60×10^{-01}	< 0.01	9.44×10^{-01}	< 0.01
TEMPERATE	GRA	ENF	1.66×10^{-13}	0.03	$< 1.00\times10^{-99}$	0.52
TEMPERATE	CRO	ENF	2.30×10^{-01}	< 0.01	$< 1.00\times10^{-99}$	0.27
TEMPERATE	EBF	ENF	6.00×10^{-03}	< 0.01	6.58×10^{-01}	< 0.01
TEMPERATE	GRA	EBF	3.53×10^{-08}	0.01	$< 1.00\times10^{-99}$	0.58
TEMPERATE	CRO	EBF	3.12×10^{-01}	< 0.01	$< 1.00\times10^{-99}$	0.26
TEMPERATE	GRA	CRO	4.58×10^{-07}	0.01	1.85×10^{-44}	0.09
CONTINENTAL	DBF	DNF	2.03×10^{-29}	0.06	9.89×10^{-10}	0.02
CONTINENTAL	GRA	DNF	4.91×10^{-11}	0.02	$< 1.00\times10^{-99}$	0.46
CONTINENTAL	DBF	ENF	5.96×10^{-32}	0.07	1.55×10^{-04}	0.01
CONTINENTAL	GRA	ENF	3.91×10^{-12}	0.02	$< 1.00\times10^{-99}$	0.58
CONTINENTAL	CRO	DNF	6.18×10^{-08}	0.01	1.69×10^{-96}	0.20
CONTINENTAL	CRO	DBF	1.61×10^{-12}	0.03	$< 1.00\times10^{-99}$	0.30
CONTINENTAL	CRO	ENF	1.16×10^{-09}	0.02	$< 1.00\times10^{-99}$	0.35
CONTINENTAL	GRA	DBF	2.58×10^{-18}	0.04	$< 1.00\times10^{-99}$	0.31
CONTINENTAL	GRA	CRO	6.82×10^{-01}	< 0.01	8.96×10^{-05}	0.01
CONTINENTAL	ENF	DNF	9.00×10^{-01}	< 0.01	3.40×10^{-44}	0.09

Table A3. Analysis of covariance between pairs of land covers in different Köppen–Geiger climate groupings for the relationship between TROPOMI SIF and FLUXCOM GPP. ANCOVA is only performed on the intercept when the difference between slopes is not considered significant. In order to highlight areas of similarity and difference, the η^2 column, comparable to the percentage of the difference in the slope or intercept (the latter assuming equivalence of the slopes) attributable to the vegetation cover, is coloured green, yellow and red for the slope categories: $\leq 0.01, 0.02 - 0.05, > 0.05$; and the intercept categories: $\leq 0.01, 0.02 - 0.15, > 0.15$, respectively.

915   Though the slopes are similar, a reasonable proportion of the difference in the intercept of the linear relationship is attributable to the difference in vegetation covers. This difference broadly divides along the lines of herbaceous or non-woody vegetation (CRO, GRA) and woody vegetation (EBF, DBF, ENF, DNF). The intercept, which can be interpreted as the starting potential of the SIF-GPP relationship, is generally higher for woody trees (i.e. more SIF is released for a given GPP).
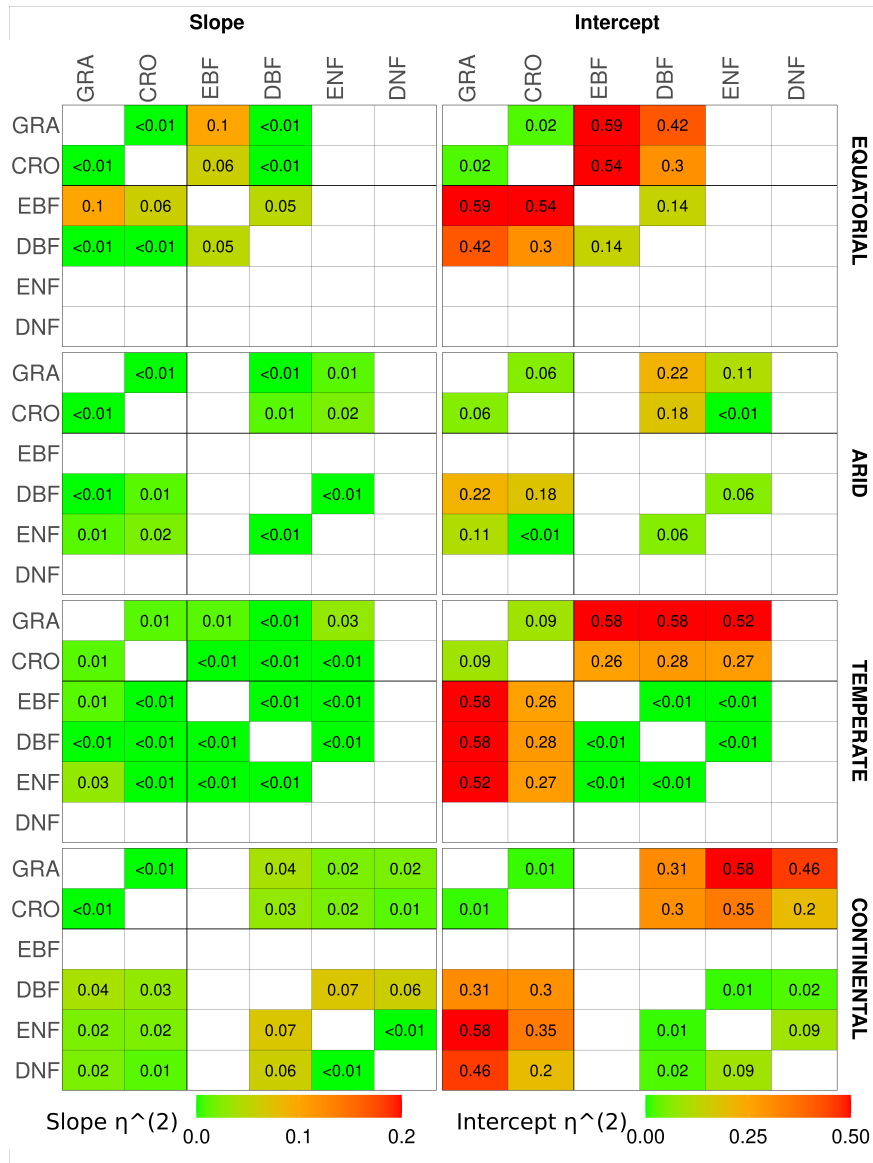
Figure A8. The η^2 parameter of an analysis of covariance between pairs of vegetation covers in different Köppen–Geiger climate groupings, for the slope (left) and intercept (right) of the linear relationship between TROPOMI SIF and FLUXCOM GPP. ANCOVA is performed on the intercept under the assumption that the difference between slopes is not significant. The η^2 parameter is comparable to the percentage of the difference in the slope or intercept (the latter assuming equivalence of the slopes) attributable to the difference in vegetation cover, with lower values signifying a smaller difference between vegetation covers. A slightly bolder line is used to separate the herbaceous species (CRO, GRA) from the woody species (EBF, DBF, ENF, DNF).